



Analysis of a saline dust storm from the Aralkum Desert - Part 1: Consistency of multisensor satellite aerosol products

Xin Xi¹, Jun Wang², Zhendong Lu², Andrew Sayer^{3,4}, Jaehwa Lee^{3,5}, Robert Levy³, Yujie Wang^{3,4},
Alexei Lyapustin³, Hongqing Liu^{6,7}, Istvan Laszlo^{6,8}, Changwoo Ahn^{3,9}, Omar Torres³,
Sabur Abdullaev¹⁰, and Ralph Kahn¹¹

¹Department of Geological and Mining Engineering and Sciences, Michigan Technological University, Houghton, MI, USA

²Department of Chemical and Biochemical Engineering, The University of Iowa, Iowa City, IA, USA

³NASA Goddard Space Flight Center, Greenbelt, MD, USA

⁴Goddard Earth Sciences Technology and Research (GESTAR) II, University of Maryland, Baltimore County, Baltimore, MD, USA

⁵Earth System Science Interdisciplinary Center, University of Maryland, College Park, MD, USA

⁶Center for Satellite Applications and Research, National Environmental Satellite, Data, and Information Service, National Oceanic and Atmospheric Administration, College Park, Maryland, USA

⁷I. M. Systems Group, Inc., College Park, Maryland, USA

⁸Department of Atmospheric and Oceanic Sciences, University of Maryland, College Park, Maryland, USA

⁹Science Systems and Applications Inc., Lanham, MD, USA

¹⁰Physical Technical Institute of the Academy of Sciences of Tajikistan, Dushanbe, Tajikistan

¹¹Laboratory for Atmospheric and Space Physics, The University of Colorado Boulder

Correspondence: Xin Xi (xinxi@mtu.edu)

Abstract. The performance and consistency of satellite observations in characterizing the saline dust emission from the newly formed Aralkum Desert have remained poorly understood. We address this knowledge gap by providing a review of satellite techniques capable of detecting the presence, column burden, and vertical height of airborne dust over desert surfaces. Then we evaluate the consistency between different aerosol products in observing an intense Aralkum dust storm in 2018, via synergistic analyses of the ultraviolet aerosol index (UVAI) from OMPS, TROPOMI and EPIC, aerosol optical depth (AOD) from MODIS and VIIRS, and aerosol optical centroid height (AOCH) from CALIOP and EPIC. The UVAI products consistently delineate the areal extent of the freshly emitted dust plume if the dynamic range of each product is considered. The heavy dust plume is however erroneously masked as clouds in the AOD products. All UVAI products show large positive values over the Garabogazköl gulf and northern Caspian Sea due to enhanced UV absorption by turbid and saline waters, suggesting that caution must be taken to avoid misinterpreting the surface effect as dust signal over ephemeral or dried lakes. The AOD products show generally good agreement in observing the total and coarse-mode AOD associated with the dust outflow to Caspian Sea. Over-land AOD retrievals show strong non-linear relationships between aerosol algorithms. The NOAA Enterprise Processing System (EPS) product yields significantly lower AOD than other algorithms, likely due to the misuse of an urban aerosol optical model for dust retrieval. The EPIC AOCH retrieval shows the best agreement with CALIOP over heavy dust burden areas, with both mean bias and RMSE below 0.5 km. This study reveals significant inconsistency between satellite aerosol products and the potential of multi-sensor approaches for identifying the product biases and limitations in Central Asia.



1 Introduction

Following the drying of Aral Sea over the past several decades, the newly formed Aralkum Desert has emerged as a major source of wind-blown saline dust aerosol, causing a range of adverse impacts on the biodiversity, agriculture, and human well-being across Central Asia (Orlovsky and Orlovsky, 2001; Abuduwaili et al., 2010; Xi and Sokolik, 2016). Aralkum stands out among the vast drylands of Central Asia, not only due to its anthropogenic origin but also for the distinct chemical and mineralogical composition of the erodible sediments. The Earth Surface Mineral Dust Source Investigation (EMIT) instrument reveals that Aralkum contains more abundant carbonate and sulfate minerals, but less iron oxides and clays than the adjacent sandy deserts (such as Karakum and Taklamakan deserts) (Fig. 1). Past studies confirmed that dust samples collected near Aralkum contained significantly higher sulfate and chloride content than those near sandy deserts (Groll et al., 2013, 2019). Hence, the dust aerosol originating from Aralkum Desert is expected to be more hygroscopic and less light-absorbing compared to typical desert dust (Rudich et al., 2002). Even within the Aralkum Desert, there is substantial intra-basin variability in the physiochemical properties of the dust-producing sediments. As the Aral Sea continued shrinking, the sediment grain size became progressively smaller towards the lowest point of the basin, while evaporate minerals started to precipitate following a typical sequence of calcite, gypsum/anhydrite, halite, and finally potassium and magnesium minerals. Consequently, distinct spatial gradients in the mineralogical composition and abundance, grain size, and soil texture have been observed over the Aral basin (Indoitu et al., 2015; Singer et al., 2001, 2003; Jiang et al., 2021). For example, Argaman et al. (2006) found that the highly erodible takyr soils dominate the outer rim of Aralkum, whereas the newly formed solonchak soils are more likely protected by salt crusts forming stable, coarse aggregates. Jiang et al. (2021) reported an increasing abundance of clay and evaporites minerals and decreasing abundance of carbonates and organic carbon from the older coasts towards the newly exposed seabed.

Quantifying the environmental impact associated with aeolian dust from Aralkum is greatly hampered by the lack of in situ measurements of the spatially heterogeneous physical and chemical properties of the erodible sediments (e.g., soil texture, mineralogical composition, crusting), and of the airborne dust particles (e.g., particle size distribution, shape, nonsphericity, chemical composition or refractive index, mixing state, solubility). In particular, the global ground network of sun/sky photometers, AERosol RObotic NETwork (AERONET), has no operating sites near the Aralkum Desert, presumably because of the region's remoteness and uninhabitable condition (Holben et al., 1998). The closest AERONET site is located 1000 km away in the capital city of Tajikistan (Dushanbe) in a mountainous region with persistent urban pollution (Rupakheti et al., 2020). AERONET measurements serve two important purposes. First, AERONET provides the climatological aerosol information needed to specify the season- and region-dependent aerosol optical models in satellite aerosol algorithms (Dubovik et al., 2002). Thus, the prevailing aerosol properties over Aralkum may be insufficiently represented in aerosol retrieval algorithms. Second, AERONET measurements are used as ground truth for evaluating the regional biases of satellite aerosol retrievals, which in turn help identify algorithm deficiencies and areas that need improvement. In general, satellite algorithms are optimized for global performance, but may be subject to significant local biases, if the local aerosol microphysical properties deviate substantially from the algorithm assumptions.

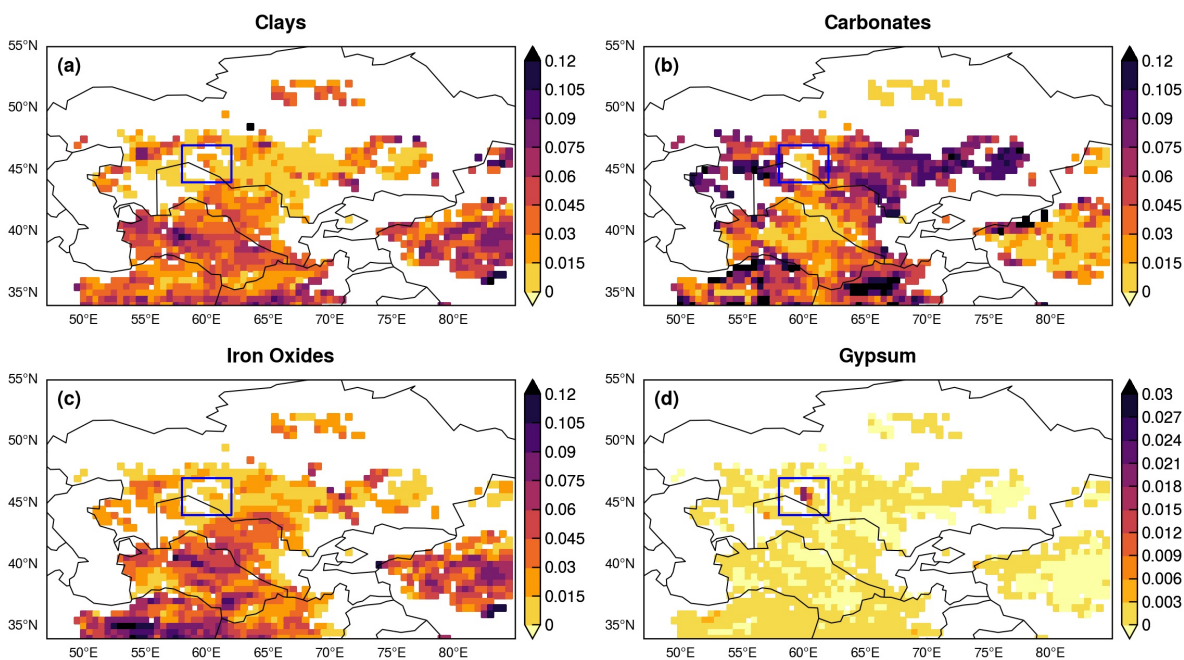


Figure 1. Aggregated spectral abundance of four mineral groups based on the Earth Surface Mineral Dust Source Investigation (EMIT) L3 product: (a) Clays (including chlorite, illite, muscovite, kaolinite, montmorillonite and vermiculite); (b) Carbonates (calcite and dolomite); (c) Iron Oxides (goethite and hematite); and (d) Gypsum. The boxed region indicates the Aralkum Desert. Note that panel (d) uses a different color scale from others.

Characterization of large-scale dust variability has primarily relied on spaceborne observations over the major continental outflow regions, such as the tropical Atlantic, North Pacific, and Arabian Sea (Yu et al., 2020). For mid-latitude drylands located in the interior of continents (such as Central Asia), observing airborne dust from space is a challenging task due to the difficulty of separating the influence of land surfaces from the top-of-the-atmosphere (TOA) radiance measurements. Central Asia comprises a diversity of dust sources, including sandy and hilly deserts, steppes, salt flats, and ephemeral water bodies (Xi and Sokolik, 2015a, b). The heterogeneous and bright surfaces pose a major challenge for retrieving the aerosol properties in the visible and near-infrared (NIR) wavelengths. A number of satellite techniques and products have been developed to facilitate aerosol monitoring over desert areas. Data users may struggle with the product choice, not knowing the strengths and limitations of different products when applied to their region of interest. In this regard, a multisensor approach is preferred over the use of a single product, especially for desert areas where aerosol remote sensing is subject to greater uncertainties than over remote oceans. So far, there is poor understanding of the performance and consistency of satellite aerosol products in observing the saline dust from the Aralkum Desert.

During 27–29 May 2018, an intense dust storm occurred from the Aralkum Desert due to cold air outbreak from the polar latitudes, causing persistent haze, record high particulate concentration, and salt deposition on cotton and food crops (Xi, 2023).



65 This event was described as “raining salt” in the media, due to the high salt content in the lofted particles (Radio Free Europe
Radio Liberty, 2018). This paper documents the first part of a detailed analysis of the saline dust storm, and investigates the
consistency of multi-sensor satellite aerosol products in detecting the presence, column burden, and vertical height of airborne
dust from the Aralkum Desert. A companion paper will focus on the atmospheric dynamics and model simulations of the event.
In this paper, we first provide a review of current satellite remote sensing techniques with aerosol observation capability over
70 desert regions (such as Central Asia) (Section 2). Specifically, the review focuses on the physical principles and algorithm
treatment of aerosol and land surface properties associated with the retrieval of three aerosol parameters: ultraviolet aerosol
index (UVAI), mid-visible aerosol optical depth (AOD), and aerosol optical centroid height (AOCH). The review provides
insight into the inherent differences between different aerosol algorithms, including the algorithms designed to retrieve the
same aerosol parameter from the same sensor. Then, we perform an intercomparison of multiple UVAI, AOD, and AOCH
75 products to examine the cross-sensor and cross-algorithm consistency in observing the Aralkum dust storm of May 2018
(Section 3). Due to the lack of ground truth, we are unable to evaluate the accuracy of the AOD products. Instead, we focus on
the consistency (or lack thereof) between different sensors, platforms, and algorithms, and explore the synergistic use of multi-
sensor data to identify possible limitations and biases in the aerosol products. The major findings of the study are summarized
in Section 4.

80 2 Review of Aerosol Remote Sensing Over Desert Areas

2.1 UVAI

2.1.1 Overview

In the near UV wavelengths (330–380 nm) where ozone absorption is weak, the TOA upwelling radiance consists of contribu-
tions from molecular scattering, scattering and absorption by clouds and aerosols, and surface reflection. The low reflectivity
85 of snow-free land surfaces in the UV allows the separation of the atmospheric contribution (called path radiance) from sur-
face reflection (Herman and Celarier, 1997). The aerosol detection capability in the near UV spectrum was first discovered
as a spectral residual quantity in the Total Ozone Mapping Spectrometer (TOMS) ozone algorithm, which assumes that the
aerosol and cloud scattering and surface reflection can be collectively represented as a hypothetical Lambertian reflector at the
bottom of a pure molecular atmosphere. The Lambert Equivalent Reflectivity (LER) of this “effective surface” is assumed to
90 be wavelength-independent, and determined from radiance measurements at a reference wavelength (λ_0) insensitive to ozone
absorption, based on radiative transfer calculations for a pure molecular atmosphere (Herman and Celarier, 1997). A resid-
ual quantity in the LER (or LER difference) between λ_0 and a neighboring wavelength (λ , usually shorter than λ_0), which
measures the deviation of the spectral dependence of observed UV radiances from that of a pure molecular atmosphere (gov-
erned by Rayleigh scattering), was found to be close to zero under most conditions. Significant LER differences between λ_0
95 and λ , however, were frequently found to coincide with the presence of UV-absorbing aerosols, such as dust, carbonaceous



aerosol, and volcanic ash (Hsu, 1996; Herman et al., 1997). Because of the predominant association with absorbing aerosols, the spectral residual quantity has been referred to as UVAI, or Absorption Aerosol Index (AAI).

The computation of UVAI involves minimal a priori information about aerosol properties, but highly depends on the calibration accuracy at the two wavelengths involved. Historically, two wavelength pairs have been used: 340/380 nm and 354/388 nm, of which the longer wavelength is used as the reference wavelength λ_0 . In the original UVAI definition, clouds were treated as part of the Lambertian reflector in Rayleigh scattering calculations. This LER-based UVAI yields small negative values for clouds and non-absorbing aerosols. Torres et al. (2018) introduced a new approach by explicitly treating the scattering effects of water clouds based on Mie theory. The Mie-based UVAI was found to be closer to zero over cloudy scenes, and have weaker angular dependence compared to the LER-based UVAI.

UVAI yields large positive values in the presence of absorbing aerosols, including over deserts, snow, or ice-covered areas, and above clouds (Torres et al., 2012). This makes UVAI an excellent tracer of airborne dust. For example, the TOMS UVAI product was used for tracking dust transport and mapping dust sources, which established the basis for the empirical dust source function used in global dust models (Prospero et al., 2002). Compared to a pure Rayleigh scattering atmosphere, dust reduces the spectral contrast of backscattered UV radiances through the absorption of Rayleigh scattered radiation from beneath the aerosol layer (Herman et al., 1997; Torres et al., 1998; de Graaf et al., 2005). In addition, dust is generally more absorbing at shorter wavelengths, which further enhances the deviation of the spectral dependence of backscattered radiances from that of a Rayleigh scattering atmosphere (Sokolik and Toon, 1999). For an aerosol layer, its UVAI value is closely related to the AOD, vertical height, absorption capability (i.e. single scattering albedo) and surface albedo (de Graaf et al., 2005). The more elevated an aerosol layer, the higher the UVAI, holding other things equal. It also means that assumptions or a priori information about the aerosol height and type are required to estimate AOD from UVAI (Torres et al., 2013).

Despite the unique capability of UVAI in detecting absorbing aerosols over various surface types, it should be noted that some geophysical effects can cause large UVAI values similar to the effects of aerosols, such as sun glint, ocean color, and the wavelength dependence of surface reflectance that violates the spectrally independent LER assumption (Herman and Celarier, 1997). These effects, if misinterpreted as aerosol signal, will introduce errors in inferring dust properties and sources from UVAI.

UVAI products has been generated from a number of spaceborne UV-visible spectrometers, including TOMS, Global Ozone Monitoring Experiment (GOME), Scanning Imaging Absorption Spectrometer for Atmospheric Cartography (SCIAMACHY), Ozone Monitoring Instrument (OMI), Ozone Mapping and Profiler Suite (OMPS), and TROPOspheric Monitoring Instrument (TROPOMI). Below we briefly describe the instruments considered in this study.

2.1.2 OMI

OMI is a nadir-looking grating spectrometer that operates onboard the Aura spacecraft in a sun-synchronous orbit with an ascending node equatorial crossing time of 13:38. OMI measures upwelling radiances in three channels: UV-1 (264–311 nm), UV-2 (307–383 nm) and VIS (349–504 nm) with a footprint size of $13 \times 24 \text{ km}^2$ at nadir. The OMI near-UV aerosol algorithm (OMAERUV) reports the Mie-based UVAI at the 354/388 nm wavelengths (Torres, 2006). Unfortunately, OMI suffered a row



130 anomaly issue since 2008 (Torres et al., 2018), which significantly reduced the data coverage and thus is not included in our analysis.

2.1.3 OMPS

The OMPS Nadir Mapper is an imaging spectrometer that operates onboard the Suomi National Polar-orbiting Partnership (SNPP) spacecraft in a sun-synchronous orbit with an ascending node equatorial crossing time of 13:30. OMPS measures UV
135 radiances every 0.42 nm from 300 to 380 nm with a nadir footprint size of 50×50 km² and 110° across-track field of view, equivalent to a ground swath of 2800 km. The OMPS Nadir Mapper aerosol algorithm (NMMIEAI) reports the Mie-based UVAI at the 340/378.5 nm wavelengths (Torres, 2019a).

2.1.4 TROPOMI

TROPOMI is a nadir-viewing, push-broom-type grating spectrometer deployed on the Copernicus Sentinel 5 Precursor (S5P)
140 mission, which flies in close formation with the SNPP spacecraft (less than 5 min apart) in a sun-synchronous orbit with an ascending node equatorial crossing time of 13:30 (Veefkind et al., 2012). TROPOMI measures reflected and emitted radiation in the UV-visible (270–500 nm), NIR (710–770 nm), and shortwave infrared (SWIR, 2314–2382 nm) wavelengths with a footprint size of 3.5×7 km² at nadir.

There are two separate UVAI products from TROPOMI, one developed by Royal Netherlands Meteorological Institute
145 (KNMI) and European Space Agency (ESA), and the other developed by the National Aeronautics and Space Administration (NASA). The ESA version reports LER-based UVAI at two wavelength pairs: 354/388 nm and 340/380 nm (Stein Zweers, 2022). The NASA version is based on the TropOMAER aerosol algorithm, and reports both LER- and Mie-based UVAI at the 354/388 nm wavelengths (Torres, 2021).

2.1.5 EPIC

150 EPIC is an imaging spectroradiometer onboard the Deep Space Climate Observatory (DSCOVR) spacecraft, and measures the Earth's reflected solar radiance in ten narrow channels spanning from UV to NIR (317–779 nm), with a spatial resolution of 8 km at 443 nm and 16 km in other bands (Marshak et al., 2018). DSCOVR operates in a Lissajous orbit about Lagrange-1 point in the Earth-Sun system, which allows EPIC to view the sunlit disk of Earth every 60–100 minutes. The EPIC EPICAERUV aerosol algorithm reports both LER- and Mie-based UVAI at the 340/388 nm wavelengths (Torres, 2019b).

155 2.2 AOD

2.2.1 Overview

Unlike UVAI which is a qualitative tracer of absorbing aerosols, mid-visible (usually at 0.55 μm) AOD provides a quantitative measure of the aerosol burden in the atmospheric column. Inferring AOD from reflected sunlight by the surface-atmosphere system is an ill-posed inverse problem and must rely on a priori knowledge or assumptions on the aerosol microphysical



160 properties, known as aerosol optical models. The aerosol optical models are characterized by unique combinations of particle
size distribution, shape, and composition (or refractive index). A general strategy of AOD retrieval from passive, downward-
looking sensors involves using a forward radiative transfer model to compute the TOA spectral reflectances for a set of pre-
defined aerosol optical models, surface types, and solar/viewing geometries expected to be encountered by the instruments
(Remer et al., 2013a). During the AOD retrieval, the pre-calculated reflectances, which are stored in look-up tables (LUTs),
165 are compared against measured TOA reflectances to find the best fit and solution for AOD and additional parameters related
to particle size and absorption. Aerosol retrieval using this method is highly sensitive to the predefined aerosol models, which
aim to represent the aerosol conditions encountered by the sensor as realistically as possible, and ultimately determine the
AOD spectral dependence (i.e. Angström Exponent) and single scattering albedo (SSA). The predefined aerosol models are
commonly determined from long-term sun/sky photometer measurements and/or field campaign measurements, and typically
170 represent the prevailing aerosol conditions at different locations and seasons (Dubovik et al., 2002). However, different aerosol
algorithms may include inconsistent, sometimes conflicting, assumptions of the aerosol properties, causing disparities between
satellite products and between satellite observations and aerosol models.

Below, we briefly review the AOD algorithms implemented in the Moderate Resolution Imaging Spectroradiometer (MODIS)
and Visible Infrared Imaging Radiometer Suite (VIIRS) sensors. The Dark Target (DT), Multi-Angle Implementation of Atmo-
spheric Correction (MAIAC), and Deep Blue (DB) algorithms are suitable for observing dust outflow over major water bodies,
175 such as the Caspian Sea. The DB, MAIAC, and Enterprise Processing System (EPS) algorithms are capable of retrieving AOD
over desert surfaces. The review focuses on the treatment of aerosol optical models and spectral surface reflectances in different
algorithms. Other algorithm processes, such as the screening of sun glint/snow/clouds, are not discussed. A detailed review
of the treatment of dust microphysical properties in satellite algorithms and global models was recently given by Castellanos
180 et al. (2024).

2.2.2 DT algorithm

The DT algorithm exploits the contrast of reflective aerosol layers against a dark background in the visible spectrum. Over
ocean, the algorithm searches the LUT for the best fit of the measured TOA reflectances at seven window bands from visible
to SWIR, and obtains solutions for both AOD and fine mode fraction (FMF) at $0.55 \mu\text{m}$ (Tanré et al., 1997). The algorithm
185 assumes that the ambient aerosol scene can be represented as a linear combination of one fine mode and one coarse mode
weighted by FMF, out of 20 possible combinations of four fine-mode and five coarse-mode aerosol models (Remer et al.,
2005). The aerosol models are derived from long-term AERONET measurements near water bodies. Two of the five coarse
models represent dust aerosol, with the refractive index and size distribution based on observed airborne dust. Due to lack
of non-spherical dust models, the algorithm was known to generate biased retrievals over dusty oceanic regions (Zhou et al.,
190 2020b). Recently, a spheroidal dust model was introduced to improve retrieval for dusty conditions (Zhou et al., 2020a).

Over land, the DT algorithm uses three bands (0.47 , 0.65 , and $2.11 \mu\text{m}$ for MODIS; 0.49 , 0.67 , and $2.25 \mu\text{m}$ for VIIRS) in
which the surface reflectivity of vegetated lands is still low (Kaufman et al., 1997a). The algorithm assumes a number of fine-
and coarse-dominated aerosol models, which are prescribed as a function of season and location based on cluster analysis of



the AERONET climatology (Levy et al., 2013). The algorithm accounts for the surface contribution to the TOA reflectances
195 based on empirical relationships between the visible and SWIR (2.11 or 2.25 μm) surface reflectances, which are applicable
for dark surfaces only (Kaufman et al., 1997b; Remer et al., 2005). Because the assumed visible-to-SWIR reflectance ratios do
not apply for bright desert areas, the DT algorithm provides very limited coverage near dust source areas.

2.2.3 DB algorithm

Inspired by the aerosol observation capability in the near-UV, the DB algorithm employs the 0.41 μm or “deep blue” band,
200 which has lower and more homogeneous surface reflectivity than the longer visible wavelengths and thus provides sufficient
contrast between the surface and aerosol signals (Hsu et al., 2004). Over land, the algorithm uses three bands: deep blue
(0.41 μm), blue (0.47 μm for MODIS, 0.49 μm for VIIRS), and red (0.65 μm for MODIS, 0.67 μm for VIIRS). Initially
implemented to fill the gap over bright surfaces (including deserts), the algorithm considered an aerosol optical model with
an empirical scattering phase function that matched the AERONET measurements at Cape Verde. These were later replaced
205 with a spheroidal dust model and a spherical fine-dominated anthropogenic model, while the algorithm is expanded to the
entire land surfaces not influenced by cloud, snow, or ice. The dust/anthropogenic optical models are created for various SSA
values, which are prescribed for specific locations and seasons. Note that the MODIS DB product used in this study dose not
include the aerosol optical model update (Hsu et al., 2013), while the VIIRS DB product does (Lee et al., 2024). The surface
reflectance is determined based on a pre-calculated database over bright surfaces (e.g., deserts, urban areas), and empirical
210 surface reflectance relationships between the visible and SWIR bands (similar to the DT approach) as a function of normalized
difference vegetation index (NDVI) over vegetated areas (Hsu et al., 2013).

Over ocean, the DB algorithm began to generate AOD retrieval from VIIRS based on the Satellite Ocean Aerosol Retrieval
(SOAR) algorithm (Sayer et al., 2018). SOAR considers four aerosol optical models over water: maritime, dust, fine-dominated,
and mixed, each represented as a bi-modal distribution of one fine and one coarse modes. The dust model consists of one
215 spherical fine mode and one spheroidal coarse mode, which currently is derived from AERONET measurements at Cape Verde
(Lee et al., 2017).

2.2.4 EPS algorithm

NOAA has developed a suite of aerosol products from the new-generation polar-orbiting (e.g., VIIRS) and geostationary (e.g.,
Advanced Baseline Imager) sensors using the EPS algorithm. Here we focus on the VIIRS EPS AOD product, described in
220 Laszlo (2018) and more recently Laszlo and Liu (2022).

Over ocean and inland water, the EPS algorithm is based on the MODIS heritage. The aerosol column is represented as a
linear combination of one spherical fine and one spherical coarse mode, selected from four fine mode and five coarse mode
candidate models, weighted by varying fractions of the fine mode (FMF). The aerosol models are based on the same models
considered in the MODIS DT algorithm (Remer et al., 2006). The algorithm searches for the AOD and FMF that give the
225 best match between observed and pre-calculated TOA reflectances at seven VIIRS channels (M4, M5, M6, M7, M8, M10, and

M11) (Jackson et al., 2013; Laszlo and Liu, 2022). The surface contribution to the TOA reflectance is represented as a sum of bi-directional sun-glint and Lambertian underwater and whitecap reflection.

Over land, the EPS algorithm simultaneously retrieves AOD, aerosol model, and Lambertian surface reflectances in selected bands, by matching observed and calculated TOA reflectance over both dark and bright (snow-free) surfaces. Over dark land, the surface reflectance is retrieved from either the observed M5 (0.672 μm) or M11 (2.25 μm) band TOA reflectance, followed by estimation of surface reflectances in other bands using predetermined relationships between surface reflectances in bands M1, M2, M3, M5 and M11. The relationships are functions of observation geometry and surface type. Over bright lands, the surface reflectance is estimated from a static database of M1/M5, M2/M5 and M3/M5 reflectance ratios that are functions of the scattering angle (Zhang et al., 2016). During the retrieval process, the EPS algorithm tries four candidate models, of which three are fine-mode dominated aerosols with spherical shapes (labeled as generic, urban, and smoke) and one is coarse-mode dominated aerosol with non-spherical shape (labeled as dust). The exception is the surface region of North Africa and the Arabian Peninsula where the algorithm uses only the dust model since that is the most dominant aerosol type and because the dynamic model selection is impaired by the bright surface. The candidate aerosol models are adopted from the Collection 5 MODIS DT algorithm (Remer et al., 2006; Levy et al., 2007).

2.2.5 MAIAC algorithm

The MAIAC algorithm uses the dynamic minimum reflectance method to define the surface reflectance spectral ratios for each 1 km grid cell, which allows AOD retrievals over dark and bright surfaces at a high spatial resolution ($1 \times 1 \text{ km}^2$). MAIAC also uses a sliding window technique to accumulate up to 16 days of multi-angle measurements from different orbits for the same location to retrieve bidirectional surface reflectance over land (including deserts) (Lyapustin et al., 2018). The C6.1 MAIAC uses nine aerosol optical models derived from AERONET data climatology analysis to represent the regional background aerosol conditions. For Central Asia, the background aerosol model (“Model 2”) is derived from AERONET measurements over western USA, and represents a mixture of dust and fine mode aerosols. During the retrieval, a smoke/dust test is applied to determine whether the background or dust model should be used in the retrieval. Once dust is detected, the algorithm uses a spheroidal dust model (“Model 6”) derived from AERONET measurements from the Solar Village site in Saudi Arabia (Dubovik et al., 2002, 2006).

2.2.6 Algorithm implementation in MODIS and VIIRS

Under NASA’s Earth Observing System program, the twin MODIS sensors onboard the Terra and Aqua spacecrafts have generated more than 20 years’ global aerosol records. Terra operates on a sun-synchronous orbit with a 10:30 descending node equatorial crossing time. Aqua has an ascending node equatorial crossing time of 13:30 and provides nearly coincident observations with other sensors as part of the Afternoon-train (or A-train) constellation. In the MODIS aerosol product (designated as MOD04 for Terra and MYD04 for Aqua), the DT and DB algorithms perform retrieval at a nominal resolution of $10 \times 10 \text{ km}^2$, providing data coverage over dark and bright surfaces, respectively (Levy et al., 2013). In the Collection 6 release, a finer resolution DT product was produced at a $3 \times 3 \text{ km}^2$ resolution (referred to as DT3K) to better resolve small-scale aerosol

features (Munchak et al., 2013; Remer et al., 2013b). The DT3K product uses the same DT technique, but with different pixel
260 aggregation and quality assurance (QA) rules. In addition, the MAIAC algorithm uses data from both Terra and Aqua to con-
duct aerosol retrieval at a high resolution of $1 \times 1 \text{ km}^2$ over both water and land (designated as MCD19A2) (Lyapustin et al.,
2018).

As the successor for MODIS, VIIRS currently operates on three Joint Polar Satellite System (JPSS) satellites: SNPP, NOAA-
20, and NOAA-21, which fly in sun-synchronous orbits with an ascending node equatorial crossing time around 13:30. The
265 DT algorithm has been ported to VIIRS, and performs AOD retrieval at a nominal resolution of $6 \times 6 \text{ km}^2$ (Sawyer et al., 2020).
The DB algorithm implementation in VIIRS is different from that for MODIS, and performs AOD retrieval both over ocean
and over land (Hsu et al., 2019; Lee et al., 2024). Hence, the VIIRS DB AOD product is provided as an alternative to the VIIRS
DT AOD product. In addition to the DB and DT products from NASA, the NOAA EPS AOD product is another alternative for
the VIIRS sensors, and performs retrieval at the pixel level with a resolution of $0.75 \times 0.75 \text{ km}^2$ (Laszlo and Liu, 2022).

270 2.3 AOCH

2.3.1 Overview

Aerosol vertical distribution affects the atmospheric lifetime and impact of aerosols, and is an essential input for various
applications, such as retrieving AOD from UVAI and estimating ambient $\text{PM}_{2.5}$ concentration from AOD (Li et al., 2015;
Sun et al., 2019). The vertical height of absorbing aerosols (such as dust) is of particular interest for weather and climate
275 research, due to their radiative impact on the atmospheric thermodynamics and stability (Samset et al., 2018). Currently,
the retrieval of aerosol vertical distribution is obtained from both active and passive sensors. Active sensors, such as the
spaceborne lidars onboard the Cloud-Aerosol Lidar and Infrared Pathfinder Satellite Observations (CALIPSO) and Cloud-
Aerosol Transport System (CATS), provide vertically-resolved measurements of aerosol volume extinction at high vertical
resolutions (Winker et al., 2009; Yorks et al., 2016). An important limitation of spaceborne lidars, however, is their narrow
280 swath and poor spatial coverage. In recent years, there has been substantial progress in retrieving one piece information of
aerosol vertical distribution from passive sensors based on various techniques, including stereoscopic retrieval from polar-
orbiting multiangle or geostationary imagers (Nelson et al., 2013; Carr et al., 2020), polarimetric observations in the near UV
(Wu et al., 2016), differential optical absorption spectroscopy (DOAS) in the NIR (e.g., oxygen A and B bands) (Xu et al.,
2017, 2019; Chen et al., 2021), hyperspectral thermal infrared (TIR) measurements (Pierangelo et al., 2004; Peyridieu et al.,
285 2010), and the retrieval of smoke injection height from the thermal contrast of elevated smoke aerosol (Lyapustin et al., 2020).
Although passive techniques do not achieve the same level of accuracy as lidars and only estimate an effective height with
limited information on the aerosol layer geometric thickness, they provide much better spatial coverage and revisit frequency
(Lu et al., 2021, 2023).

The definition of aerosol layer height vary by different techniques, and may refer to the top of aerosol layers such as from
290 stereoscopic techniques, or an effective central height corresponding to peak aerosol extinction (Xu et al., 2017; Yorks et al.,
2023). Similar to AOD, the aerosol layer height is an optical quantity, and expected to vary with the wavelength at which they



are retrieved. Radiation at longer wavelengths is generally capable of penetrating deeper into the aerosol layer than radiation at shorter wavelengths. In addition, except for stereoscopic techniques, passive retrieval of aerosol height depends on the aerosol vertical distribution, and must rely on assumptions about the aerosol layer thickness or profile. Below, we describe two aerosol layer height products with coverage over Central Asia, including the aerosol extinction-weighted height derived from CALIPSO, and the EPIC AOC product.

2.3.2 CALIOP aerosol extinction-weighted height

As part of the A-train constellation, CALIPSO provides critical information on the vertical distribution and optical properties of aerosols and clouds. CALIPSO carries an elastic backscatter lidar, Cloud-Aerosol Lidar with Orthogonal Polarization (CALIOP), which measures polarized backscatter at 532 nm and total attenuated backscatter at 532 nm and 1032 nm, with a vertical resolution of 30 m below an altitude of 8.2 km and 60 m between 8.2 and 20.2 km (Winker et al., 2009). In the CALIOP level-2 data processing, the calibrated attenuated backscatter coefficient profiles are used to detect the top and base altitudes of atmospheric features using a selective iterated boundary location (SIBYL) algorithm. Then a set of scene classification algorithms (SCA) are used to classify these features as aerosol and cloud, and determine the aerosol type and cloud phase. During this process, the aerosol extinction-to-backscatter ratios (or aerosol lidar ratios) are selected to derive the aerosol extinction and backscatter coefficient profiles (Young et al., 2018). The lidar ratio selection relies on the aerosol typing algorithm which considers six tropospheric aerosol types: clean marine, dusty marine, dust, polluted continental/smoke, polluted dust, and elevated smoke, each assigned a default lidar ratio (Omar et al., 2009; Kim et al., 2018). The aerosol type is determined based on several input parameters: altitude, location, surface type, particulate linear depolarization ratio, and integrated attenuated backscatter. Specifically, thresholds of layer-integrated volume depolarization ratios are used to detect non-spherical aerosol types, including pure dust and dust mixtures with marine aerosol (“dusty marine”) or polluted continental aerosol (“polluted dust”) (see Fig. 2 in Omar et al., 2009). Based on the aerosol extinction profile, the CALIOP AOC with respect to the mean sea level can be computed as $\frac{\sum_{i=1}^n \beta_{ext,i} Z_i}{\sum_{i=1}^n \beta_{ext,i}}$, where $\beta_{ext,i}$ is the 532 or 1064 nm aerosol extinction coefficient (km^{-1}) at level i , and Z_i is the altitude (km) at level i (Koffi et al., 2012).

2.3.3 EPIC AOC product

The AOC retrieval from EPIC employs the oxygen absorption spectroscopic measurements in the A band near 760 nm and B band near 688 nm. The physical principle is that the enhanced scattering from elevated aerosol layers shortens the photon path length of reflected sunlight, thereby reducing its chance of being absorbed by oxygen molecules (Kokhanovsky et al., 2015; Ding et al., 2016). The oxygen A and B bands are characterized by different penetration depths of solar radiation and altitude-dependence of oxygen absorption, which establishes a basis for the AOC retrieval from the enhanced TOA reflectances compared to a pure (aerosol-free) Rayleigh scattering atmosphere (Xu et al., 2019).

The AOC retrieval algorithm employs a set of LUTs consisting of pre-computed TOA reflectances for a range of AOD, AOC, surface reflectivity, and surface pressure values for the solar/viewing geometries expected to be encountered by EPIC. Six EPIC bands are considered, including the oxygen A and B bands at 764 and 688 nm and two reference continuum bands at



325 780 and 680 nm. The aerosol vertical distribution is represented by a quasi-Gaussian profile characterized by a centroid altitude and a fixed half-width at half maxima of 1 km. The centroid altitude is reported as the aerosol layer height in the AOCH product, and represents the altitude at which the aerosol volume extinction peaks. Currently, the EPIC AOCH product considers three aerosol optical models: smoke, Saharan dust, and Asian dust. The dust models are derived from AERONET measurements at Cape Verde and over East Asia, respectively (Xu et al., 2017). The surface reflectivity is represented using different approaches
330 for water and land. The water reflectivity is based on the GOME-2 surface LER database (Xu et al., 2017), whilst the land surface reflectivity is derived from the MODIS bidirectional reflectance distribution function (BRDF) and albedo products (Xu et al., 2019). During the retrieval, the AOD is first retrieved at the EPIC window channel of 443 nm. Then the observed absorption-to-continuum band reflectance ratios or DOAS ratios, which are defined as the ratio of reflectances in the oxygen absorption bands to the reflectances in the reference continuum bands, are matched with the LUTs to find the best solutions
335 for AOCH using different spectral fitting strategies over water and land. In general, the sensitivity of DOAS ratios to AOCH is the highest for heavy aerosol burden and low surface reflectivity conditions, under which the retrieved AOCH is considered the most accurate. Whereas, the retrieved AOCH becomes less reliable when AOD decreases to nearly zero and/or surface reflection dominates the aerosol signal in the TOA reflectances.

3 Evaluation of Cross-sensor and Cross-algorithm Consistency

340 Table 1 summarizes the satellite aerosol products and parameters considered in this study. The products are selected based on data availability and are mostly from polar-orbiting sensors (except EPIC) with similar overpass time over Aralkum Desert. For the AOD products, we use the QA-screened, best estimate AOD parameters when available; otherwise we apply QA screening as recommended by each product. While some of the considered products have duplicated parameters (e.g., AOD is available from the NASA UVAI products), we focus on the primary and most widely used aerosol parameter from each product. The
345 UVAI and AOD products also report parameters related to aerosol size (e.g., Angström Exponent) and absorption (i.e. single scattering albedo); however, they are subject to larger biases and usually not recommended for use in scientific studies.

3.1 Horizontal and vertical dust distributions

In this section we describe the dust plume trajectory based on nearly coincident observations from passive and active sensors. Fig. 2 shows the daytime MODIS/Aqua true color images on 27 and 29 May 2018 and the nighttime Spinning Enhanced
350 Visible and InfraRed Imager (SEVIRI) Dust RGB composite image on 28 May 2018, along with the 532 nm total attenuated backscatter profile and AOD from three coincident CALIOP overpasses. On 27 May 2018, MODIS observed an extensive whitish dust plume off the Aralkum Desert and advancing towards Iran and Afghanistan. CALIOP missed the Aralkum dust plume, but detected a shallow dust layer (0–1 km) at the southeast coast of Caspian Sea. The dust layer was likely generated from the dry channel of ancient River Uzboy in western Turkmenistan, which has been identified as one of the most active dust
355 sources in Central Asia (Nobakht et al., 2021).



Table 1. List of satellite aerosol products considered in this study.

Sensor/Platform	Product	Parameter	Resolution	Reference
UV Aerosol Index (UVAI)				
OMPS/SNPP	NMMIEAI	UVAerosolIndex	50×50 km ²	Torres (2019a)
TROPOMI/S5P	TROPOMAER	UVAerosolIndex	7.5×3 km ²	Torres (2021)
EPIC/DSCOV	AER	UVAerosolIndex	12×12 km ²	Torres (2019b)
TROPOMI/S5P	AER	aerosol_index_340_380 aerosol_index_354_388	7.5×3 km ²	ESA (2021)
Aerosol Optical Depth (AOD)				
MODIS/Aqua	DT v6.1	Optical_Depth_Land_And_Ocean	10×10 km ²	Levy and Hsu (2015a)
MODIS/Aqua	DT3K v6.1	Optical_Depth_Land_And_Ocean	3×3 km ²	Levy and Hsu (2015b)
MODIS/Aqua	DB v6.1	Deep_Blue_Aerosol_Optical_Depth _550_Land_Best_Estimate	10×10 km ²	Levy and Hsu (2015a)
MODIS/Aqua	MAIAC v6.1	Optical_Depth_055	1×1 km ²	Lyapustin and Wang (2022)
VIIRS/NOAA20	DT v2	Optical_Depth_Land_And_Ocean	6×6 km ²	Levy et al. (2023)
VIIRS/NOAA20	DB v2	Aerosol_Optical_Thickness _550_Land_Ocean_Best_Estimate	6×6 km ²	Hsu (2022)
VIIRS/NOAA20	EPS v3r0	AOD550	0.75×0.75 km ²	Kondragunta et al. (2023)
Aerosol Optical Centroid Height (AOCH)				
CALIOP/CALIPSO	05kmAPro v4.51	Extinction_Coefficient_532 Extinction_Coefficient_1064	5 km	ASDC (2023)
EPIC/DSCOV	AOCH v1	aod, height, surf_refl	30×30 km ²	ASDC (2018)

On 28 May 2018, a high pressure system developed just to the south of Aralkum Desert, which transported the lofted dust across the Ustyurt Plateau to the Caspian Sea. The nighttime CALIOP overpass detected an extensive dust layer stretching from Aralkum to the Kopet-Dag mountain range at the Iran-Turkmenistan border. The Kopet-Dag Range acted as a physical barrier of the dust plume, causing dust particles to accumulate along the foothills resulting in high AODs up to 3. The dust layer was elevated to an altitude of 1–2 km near Aralkum, but extended to the ground surface while approaching the gently sloping foothill region. The relatively low dust layer height was probably due to the prevailing high pressure system and shallow atmospheric boundary layer during nighttime. The varying dust layer height may have explained the different color contrasts shown in the SEVIRI image. Specifically, the elevated dust displays a rich magenta color and strong contrast near the Aralkum. Whereas, the dust layer near the foothills was less discernible, possibly due to reduced temperature contrast between the ground surface and dust aloft.

On 29 May 2018, the remnants of the Aralkum dust storm continued to affect western Uzbekistan and Turkmenistan. The suspended dust was only partially detected by CALIOP due to the presence of extensive clouds above the dust. The dust layer

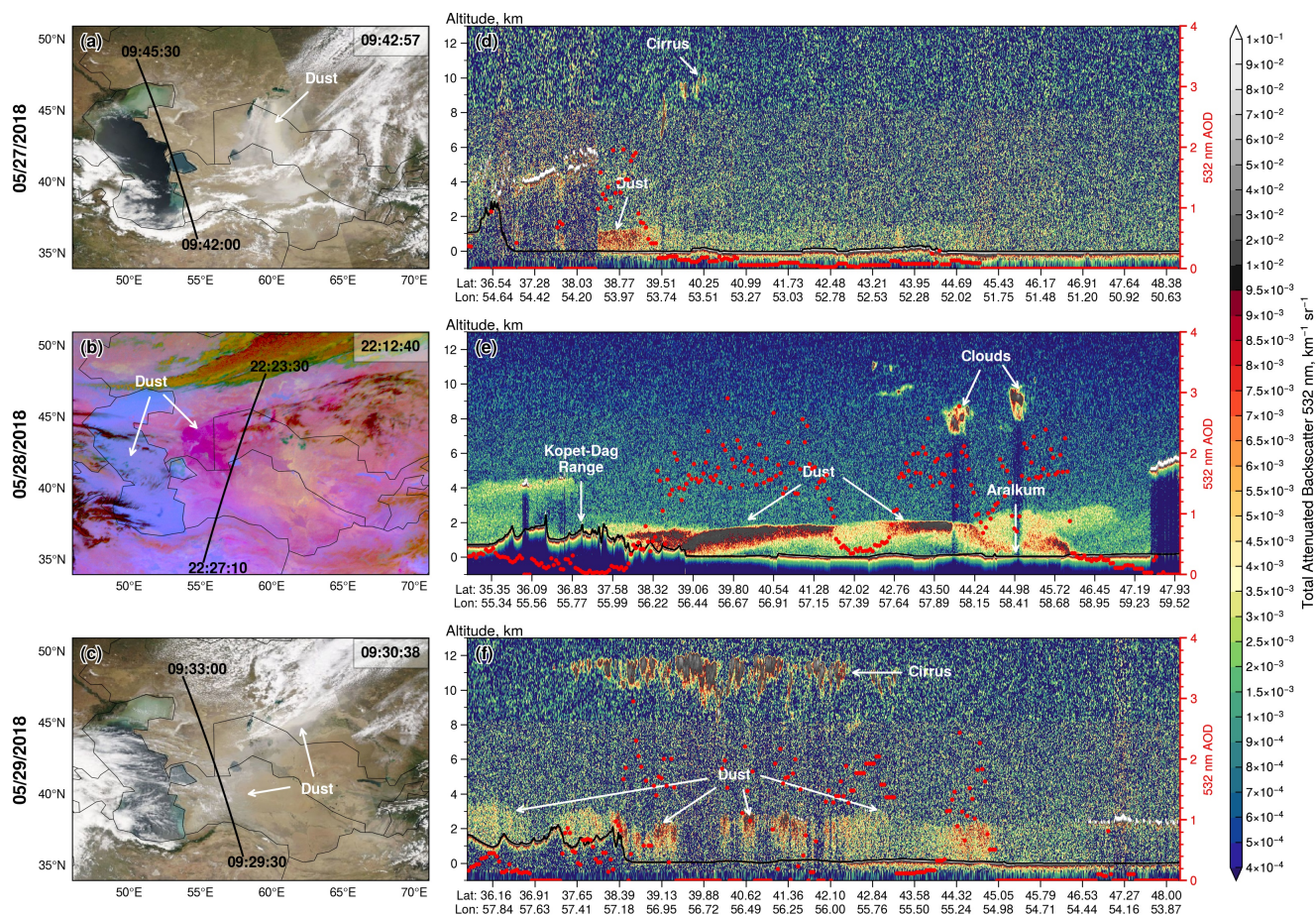


Figure 2. (a, b, c) CALIPSO ground tracks superimposed on nearly coincident MODIS/Aqua true color and SEVIRI Dust RGB composite images on 27–29 May 2018. The ground track start and end times are indicated. The MODIS or SEVIRI scan time over the Aralkum Desert (45°N, 60°E) is shown at the top right corner. (d, e, f) The corresponding CALIOP 532 nm total attenuated backscatter profile and AOD (magenta dots). Black lines indicate the ground surface.

reached an altitude of 3.5 km, likely due to convective mixing in the daytime boundary layer and enhanced vertical motion ahead of a cold front. The CALIOP-retrieved AOD was close to 2 in many areas.

370 3.2 Comparison of UVAI products

Fig. 3 compares five UVAI products in detecting the freshly emitted dust plume on 27 May 2018. The UVAI products include the Mie-based UVAI (named as “UVAerosolIndex”) from OMPS, TROPOMI, and EPIC, provided by NASA, and the LER-based UVAI from TROPOMI, provided by ESA. These sensors flew over Aralkum within a short time window (less than 20

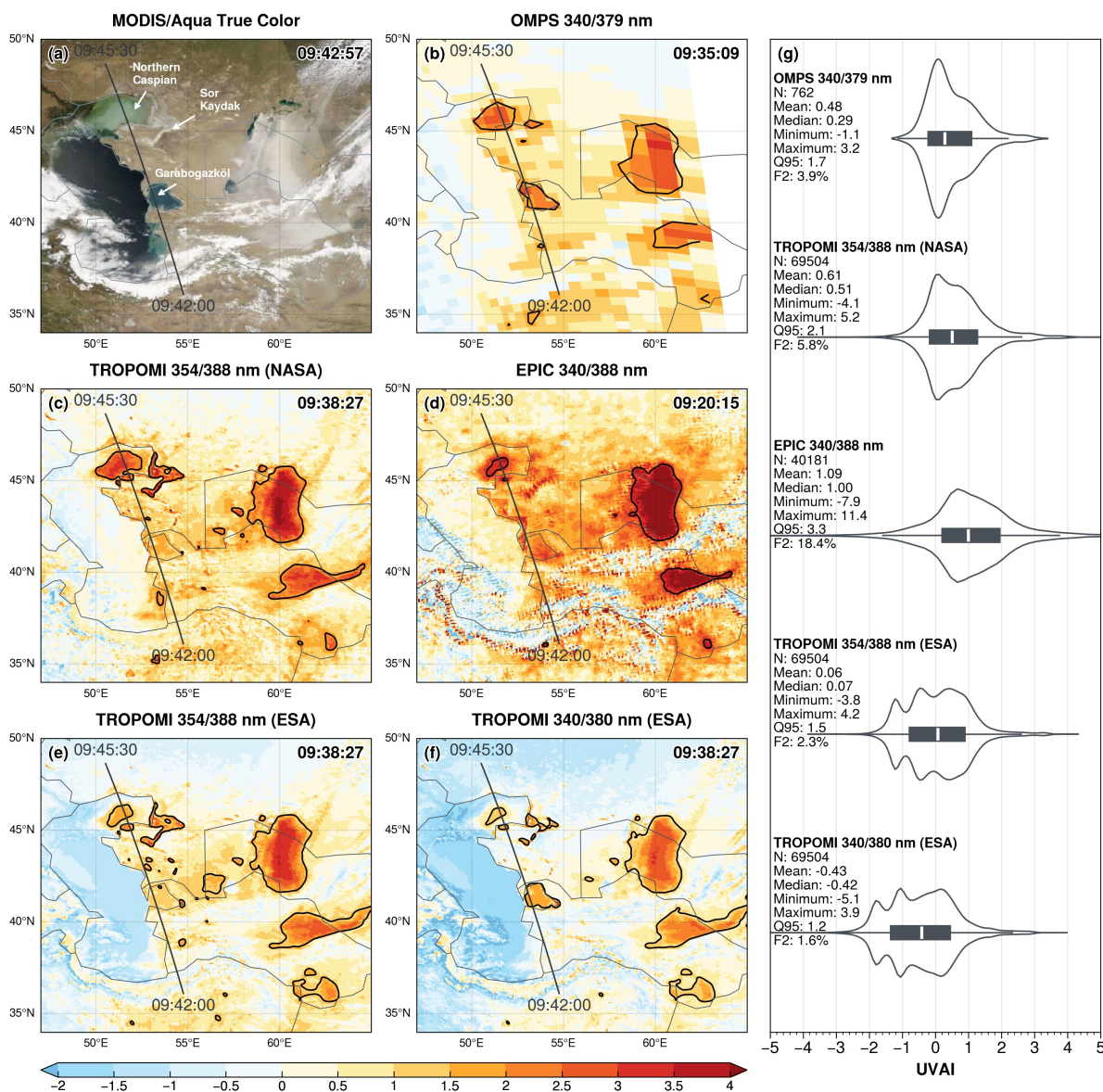


Figure 3. Comparison of five UVAI products on 27 May 2018: (a) MODIS/Aqua true color image, (b) 340/379 nm UVAI from OMPS, (c) 354/388 nm UVAI from TROPOMI (NASA), (d) 340/388 nm UVAI from EPIC, (e) 354/388 nm UVAI from TROPOMI (ESA), (f) 340/380 nm UVAI from TROPOMI (ESA), and (g) violin plots and summary statistics of the UVAI products. The instrument overpass time over the Aralkum Desert (45°N, 60°E) is shown at the top right corner of each panel. Straight lines in (a–f) indicate the CALIPSO ground track on 27 May 2018. Black contours in (b–f) indicate the 95% percentile of each product. Summary statistics in (g) include pixel count (N), mean, median, minimum, maximum, 95% percentile (Q95), and the fraction of pixels with $UVAI \geq 2$ (F2).



minutes) and thus observed the same scene. The products show similar spatial patterns associated with the dust plume, but
375 reveal significant differences in the UVAI magnitude and dynamic range.

By accounting for the cloud scattering effects, the Mie-based UVAI products from OMPS and TROPOMI (NASA) yield near
zero values for dust-free regions. Both products display a bimodal distribution with a peak around zero, and a small positive
peak close to 1 (Fig. 3g). The OMPS UVAI is generally smaller likely due to its coarser resolution and cloud influence. EPIC
yields significantly higher UVAI than OMPS and TROPOMI (NASA) for dusty scenes, partly because of the higher sensitivity
380 to absorbing aerosols in the 340/380 nm wavelengths. The cloudy scenes in EPIC appear more noisy, most likely due to EPIC
L1 calibration issues (personal communication with Karin Blank).

The LER-based UVAI products from TROPOMI (ESA) are lower than the NASA counterpart, and show large negative
values over dust-free areas. The choice of wavelength pairs (354/388 vs. 340/380 nm) has a minor effect on the shape of the
UVAI statistical distribution, both characterized by a tri-modal distribution with two negative modes and one positive mode.
385 However, the 354/388 nm UVAI is 0.5 higher than the 340/380 nm counterpart.

Satellite UVAI products have been widely used for dust plume tracking and source mapping, thanks to its ease of computation
and great coverage over desert regions. A threshold UVAI value is usually used to isolate the dust signal. For example, Prospero
et al. (2002) used a threshold of 1 for North Africa and 0.7 elsewhere. Schepanski et al. (2012) used a threshold of 2 to detect
major dust plumes over the Sahara. Based on a UVAI threshold of 2, we find that EPIC has over 18% pixels exceeding the
390 threshold, 2 to 9 times more than other products (Fig. 3g). In contrast, using a percentile threshold better represents the dynamic
range of each product and produces a more coherent detection of the dust plume. Specifically, using the 95th percentile as a
threshold for dust detection, the products show a general agreement in delineating the areal extent of heavy dust plume from
Aralkum. The plume features two major clusters of elevated UVAI values, separated by a cloud band (as seen in Fig. 3a).
Another small cluster of large UVAI values was observed over the Tejen and Murghab river deltas in southern Turkmenistan,
395 likely due to local emission or transported dust from Afghanistan.

A persistent feature in all UVAI products is the presence of large positive values along the eastern coast of Caspian Sea,
especially over the northern Caspian Sea and Garabogazköl gulf. To verify if airborne dust was responsible, we compare the
CALIOP AOD with coincident UVAI products along the overpass shown in Fig. 3. We create the co-located data by first
identifying the nearest pixels from all UVAI products to the CALIOP footprints, and then shifting the UVAI pixels along
400 track based on the sensor scan time differences. As shown in Fig. 3, CALIOP has an average time difference of 10, 6, and 23
minutes from OMPS, TROPOMI, and EPIC, respectively. The coincident AOD and UVAI retrievals are displayed in Fig. 4,
after applying a moving average every 5 seconds to smooth the data.

CALIOP detected a dust layer at the southeastern coast of Caspian Sea (see Fig. 2d) with an AOD up to 1.8. Over the
northern Caspian Sea and Garabogazköl gulf, CALIOP detected a very thin aerosol layer with negligible AOD, which may
405 be transported dust from the adjacent deserts (e.g., Ryn Desert). This thin aerosol layer, however, is unlikely to explain the
large positive UVAI (i.e. >2) found in these regions. Such high UVAI values are found to persist during dust-free days and
not change with time based on the high-cadence EPIC observations. Both the northern Caspian Sea and Garabogazköl gulf
have an average water depth of less than 10 m, and contain large bodies of turbid or salty water (Modabberi et al., 2019). The

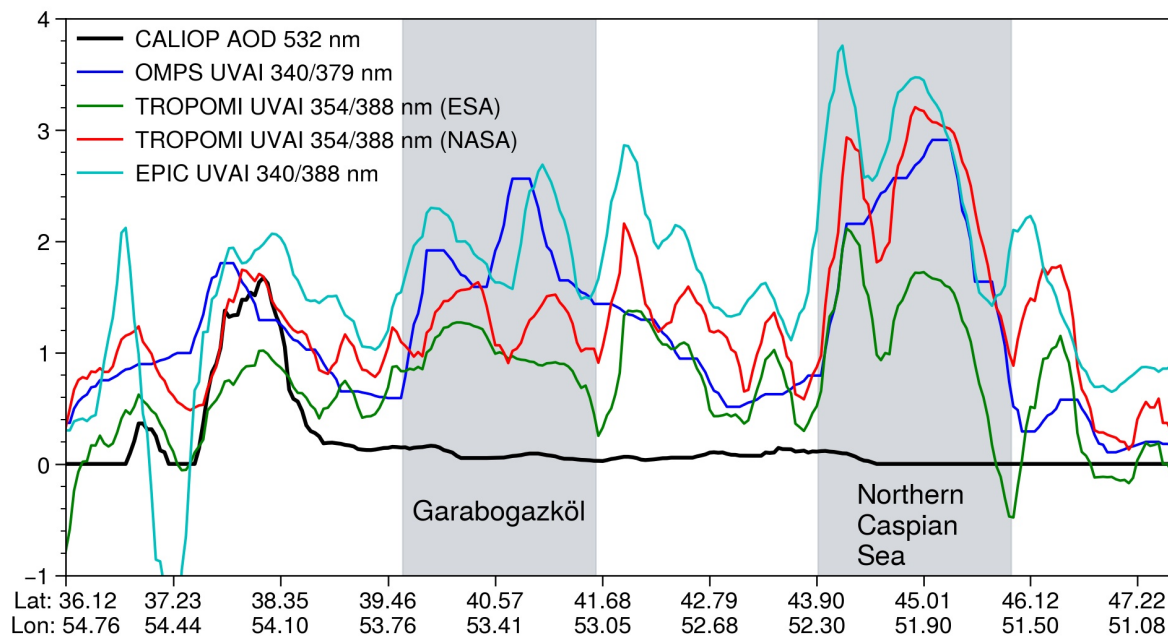


Figure 4. Comparison between CALIOP 532 nm AOD and UVAI products from OMPS, TROPOMI, and EPIC along the eastern coast of Caspian Sea on 27 May 2018. The Garabogazköl gulf and northern Caspian Sea are grayed out. The CALIPSO ground track is shown in Fig. 3.

410 persistent discoloring and turbidity of northern Caspian is caused by the influx of nutrients and sediments through the Volga and Ural rivers (Moradi, 2022). The optically active constituents in the sediment-rich water are highly absorbing in the near UV, resulting in a distinct spectral signature (i.e. stronger absorption at shorter wavelengths) similar to that of airborne dust (He et al., 2012; Lee et al., 2013; Di Biagio et al., 2019). Similarly, the highly salty water of Garabogazköl gulf (i.e. with a salinity of about 35%) causes strong UV absorption and a dust-like UVAI signal, while the main body of Caspian Sea has a much lower salinity (1.3%) and produces near zero UVAI. In addition, the Sor Kaydak salt marsh to the east of northern Caspian features
415 large positive UVAI (Fig. 3), probably due to enhanced UV absorption by salt minerals and organisms (e.g., algae). Therefore, the enhanced UV absorption of turbid and saline waters along the Caspian coast causes the water-leaving UV radiances to deviate from that of a pure scattering atmosphere, resulting in large positive UVAI similar to the effect of airborne dust. This surface effect-related UVAI signal is expected to be common over ephemeral and dried saline lakes (including Aralkum Desert), presenting a possible source of errors in using UVAI products for dust detection over these potential dust source areas.

420 3.3 Comparison of AOD products

Due to the inhomogeneous and generally higher surface reflectivity, AOD retrieval over land involves larger inconsistencies in the algorithm treatment of aerosol microphysical properties and surface reflectivity compared to AOD retrieval over water.



Table 2. Summary statistics of eight AOD products in observing the Aralkum dust event of 27–29 May 2018, based on the best quality, over-land retrievals within region 47°E–70°E, 34°N–50°N. SD, standard deviation; MAD, median absolute deviation. P95, 95th percentile.

AOD Product	N	Mean	SD	Median	MAD	Skewness	P95	Max.
MODIS/Terra DB	25,821	0.43	0.68	0.22	0.15	3.4	1.8	3.5
MODIS/Aqua DB	25,559	0.42	0.52	0.28	0.16	3.6	1.4	3.5
MODIS/Terra MAIAC	6,530,616	0.30	0.49	0.16	0.09	5.2	1.1	6
MODIS/Aqua MAIAC	6,209,626	0.33	0.63	0.15	0.08	4.7	1.3	6
VIIRS/SNPP DB	137,569	0.39	0.69	0.14	0.09	3.9	1.6	5
VIIRS/NOAA20 DB	133,199	0.49	0.80	0.20	0.14	3.5	2.0	5
VIIRS/SNPP EPS	6,179,831	0.44	0.59	0.21	0.16	2.5	1.8	5
VIIRS/NOAA20 EPS	5,311,729	0.35	0.52	0.16	0.14	2.8	1.5	5

The over-land AOD retrieval generally uses fewer spectral bands and more assumptions about region- and season-dependent aerosol conditions. In this section, we first evaluate the consistency of AOD products in observing the suspended dust over desert surfaces during 27–29 May 2018. Then, we compare the AOD products in observing the dust outflow to the Caspian Sea on 28 May 2018.

3.3.1 Dust over desert surfaces

We first report the statistical properties of eight AOD products, summarized in Table 2. The statistics are computed from the best quality, over-land retrievals from each product covering the Aral basin (47°E–70°E, 34°N–50°N) during the period of 27–29 May 2018. The number of pixels from each product varies greatly because of the different spatial resolutions, but also depends on the screening of irretrievable scenes (e.g., clouds, snow/ice, sun glint and ocean color) and the definition of retrieval quality or bias. These factors lead to inconsistent sampling by the products. The inconsistent sampling, together with different retrieval techniques (e.g., use of different aerosol optical models and surface reflectance database in the LUTs), contribute to the disparity in the AOD statistics. In addition to AOD algorithm differences, the NOAA EPS product uses L1b data from the NOAA VIIRS Calibration/Validation group, while the NASA DT and DB products use the L1b data provided by the NASA VIIRS Calibration Support Team.

Table 2 shows large variances (i.e. coefficient of variation > 1) and strong positive skewness in all products, especially the MAIAC products. The MODIS regional mean (or median) AODs are more consistent between platforms than between algorithms. Specifically, the inter-platform (Terra vs. Aqua) difference in the mean AOD is 0.01–0.03 or less than 10%, while the inter-algorithm (DB vs. MAIAC) difference is 0.09–0.13 or more than 20%. For VIIRS, the inter-platform (SNPP vs. NOAA20) and inter-algorithm (DB vs. EPS) differences are comparable. The DB algorithm yields larger variances and skewness than EPS, indicating more extreme AOD values. We find that the EPS algorithm retrieves more frequent high AODs from VIIRS/SNPP than from VIIRS/NOAA20, causing significant differences in the regional mean AODs.

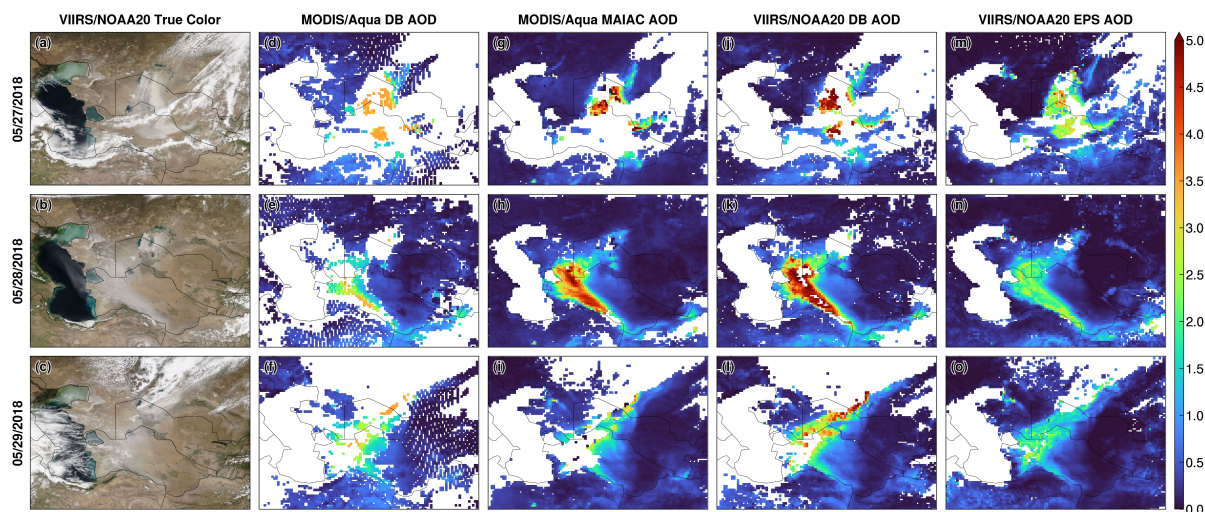


Figure 5. Multi-sensor AOD retrieval of the Aralkum dust storm on 27–29 May 2018: VIIRS/NOAA20 true color composite (a, b, c), MODIS/Aqua DB product (d, e, f), MODIS/Aqua MAIAC product (g, h, i), VIIRS/NOAA20 DB product (j, k, l), and VIIRS/NOAA20 EPS product (m, n, o). Only over-land retrievals are shown. All products are gridded to a $0.2^\circ \times 0.2^\circ$ resolution.

We further take a closer look at the DB and MAIAC products from MODIS/Aqua, and the DB and EPS products from
445 VIIRS/NOAA20. The instruments are hereafter referred to simply as MODIS and VIIRS unless otherwise specified. By comparing two different products from the same sensor, we can attribute the AOD differences to the choice of aerosol algorithms. As the AOD products are provided at different resolutions, we first regrid them onto a uniform $0.2^\circ \times 0.2^\circ$ grid, and calculate the mean value within each grid cell. The daily gridded AODs are displayed in Fig. 5, together with the VIIRS true color images which can help identify missing retrievals due to clouds or erroneous cloud screening.

450 All products failed to observe the full extent of the heavy dust plume on 27 May 2018. Among the four products, VIIRS EPS has the highest retrieval fraction. The fundamental approach of AOD retrieval from reflected sunlight relies on the brightening of the scene by aerosol scattering (primarily the forward scattering of surface reflection) against a relatively dark background. As the aerosol burden increases beyond a certain magnitude, the TOA reflectances start to flatten out and become insensitive to any additional increase in AOD. As a result, all algorithms prescribe an upper AOD limit, as shown in Table 2. Setting an
455 upper limit is necessary in order to reduce the risk of cloud contamination. The quality of retrieved AODs for heavy aerosol events tends to have large residuals and high possibility of cloud contamination. Indeed, we find that the missing retrievals in the VIIRS DB product were marked as marginal quality, and thus not included in the “best quality” estimate.

To verify if the freshly emitted dust plume on 27 May 2018 was erroneously categorized as clouds, Fig. 6 shows the cloud fraction or mask reported in selected L2 granules from each product. The TROPOMI TropOMAER UVAI is also shown to
460 indicate the dust plume location. Given the slight difference in overpass time between S5P and Aqua (5 minute apart) and between S5P and NOAA20 (1 hour apart), TROPOMI UVAI provides a nearly coincident view of the dust plume as MODIS

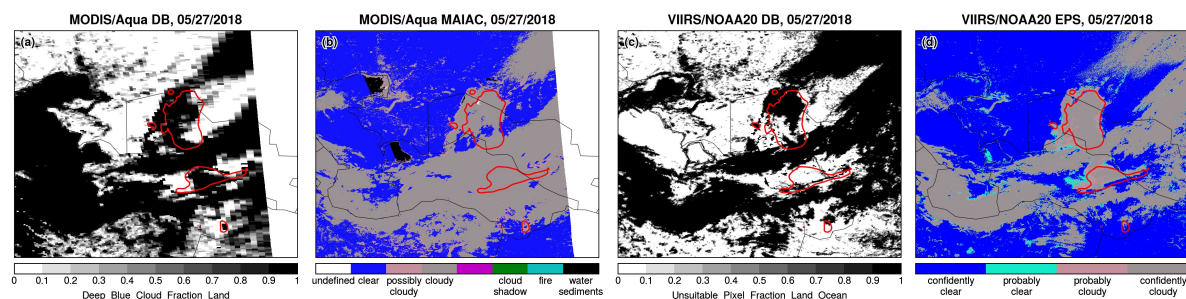


Figure 6. Mis-classification of the heavy dust plume as clouds on 27 May 2018. (a) Cloud fraction in the MODIS/Aqua DB product; (b) Cloud mask in the MODIS/Aqua MAIAC product; (c) Unsuitable pixel fraction in the VIIRS/NOAA20 DB product; and (d) Cloud mask in the VIIRS/NOAA20 EPS product. The dust plume is indicated by the TROPOMI TropOMAER UVAI value of 2 (red contours).

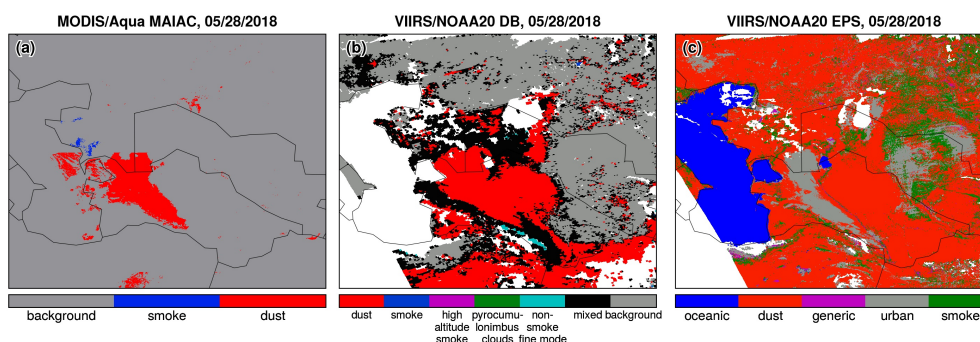


Figure 7. The aerosol optical model used for AOD retrieval on 28 May 2018 in the (a) MODIS/Aqua MAIAC, (b) VIIRS/NOAA20 DB, and (c) VIIRS/NOAA20 EPS products.

and VIIRS. Fig. 6 reveals that the majority of the heavy dust plume is classified as clouds in all products. For MODIS, the DB algorithm only detected the dust plume fringe area, where the retrieved AOD reached the algorithm limit (3.5). MAIAC classified the majority of dust pixels as “cloudy”, but it was able to see the “clear” pixels through cloud gaps. Surprisingly, MAIAC successfully detected the sediment-rich water of the northern Caspian Sea and Garabogazköl gulf. For VIIRS, the DB algorithm does not report the cloud fraction or mask, but instead report the fraction of level-1 pixels not used in the retrieval, named Unsuitable_Pixel_Fraction_Land_Ocean. This parameter shows that the dust pixels close to Aralkum were mostly excluded in the retrieval. Similarly, EPS classified most of the dust plume as “confidently cloudy”, except for the plume fringe areas where the pixels are classified as “probably clear”.

On 28 May 2018, the Aral Sea basin is influenced by a high pressure system that provided an ideal cloud-free condition for aerosol retrieval. Fig. 5 shows that all products were able to observe the extensive dust layer covering western Uzbekistan and Turkmenistan, albeit with large differences in the AOD magnitude. A striking difference among the products is that the VIIRS EPS product yields much lower (by more than 50%) AOD than others over the dust-affected region. As described

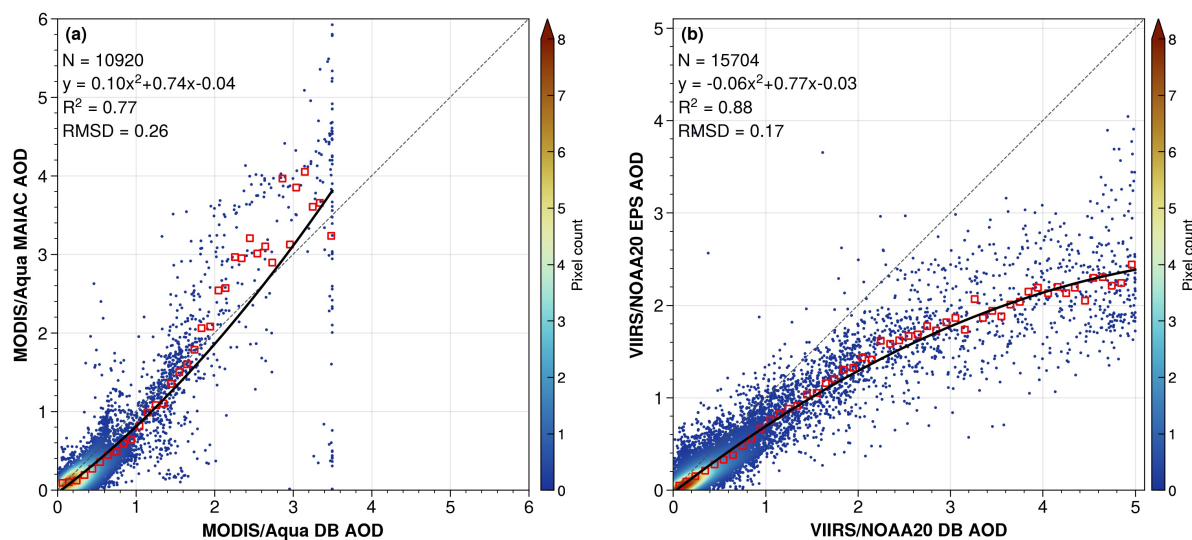


Figure 8. Comparison of over-land AOD retrieval using different algorithms during 27–29 May 2018: (a) MODIS/Aqua MAIAC vs. DB; (b) VIIRS/NOAA20 EPS vs. DB. Black lines indicate the quadratic model fits. Red squares indicate the bin-averaged AODs every 0.1 increments. RMSD, root mean square difference.

in Section 2, these aerosol algorithms use location- and season-dependent aerosol optical models for AOD retrieval over
475 land, including a coarse-dominated dust model dedicated for dust retrieval. To find out whether the dust optical model was
successfully used for retrieval on 28 May 2018, Fig. 7 displays the aerosol model used for retrieval within each product. The
MODIS DB product does not report the aerosol model information and thus is not shown. The MODIS MAIAC and VIIRS DB
products successfully selected their dust optical models for retrieval over the dusty scene in Turkmenistan. However, the VIIRS
EPS product mistakenly selected the urban aerosol model for the dusty scene. According to Laszlo and Liu (2022), the EPS
480 algorithm retrieves the AOD in the $0.41 \mu\text{m}$ channel first, which is then used to derive the AOD in other wavelengths based
on the spectral normalized extinction coefficients determined by the selected aerosol model. In the EPS algorithm, the urban
aerosol model yields a much stronger wavelength dependence in the extinction coefficient compared to the dust model (refer to
Figure 3-4 in Laszlo and Liu (2022)). Assuming the same AOD at $0.41 \mu\text{m}$, the dust model yields more than 40% higher AOD
at $0.55 \mu\text{m}$ than the urban aerosol model. Therefore, had the dust optical model be forcibly used in the retrieval, the EPS AOD
485 at $0.55 \mu\text{m}$ would have been significantly higher and brought into closer agreement with the DB and MAIAC algorithms.

Using the regridded AOD in Fig. 5, we further use regression analysis to examine the inter-algorithm AOD differences from
MODIS and VIIRS. We find that the choice of algorithms for both MODIS or VIIRS causes a non-linear relationship between
the AOD products. Hence a quadric model is used for fitting, as shown in Fig. 8. The model goodness of fit is measured by R^2
and root mean square difference (RMSD). Compared to DB, MAIAC produces lower AOD from MODIS under low aerosol
490 burden, but higher AOD under heavy burdens. For example, the MAIAC product is 36% lower than the DB product when
AOD < 1, but 22% higher when $2 < \text{AOD} < 3$. This nonlinear relationship may be partly explained by the higher resolution in

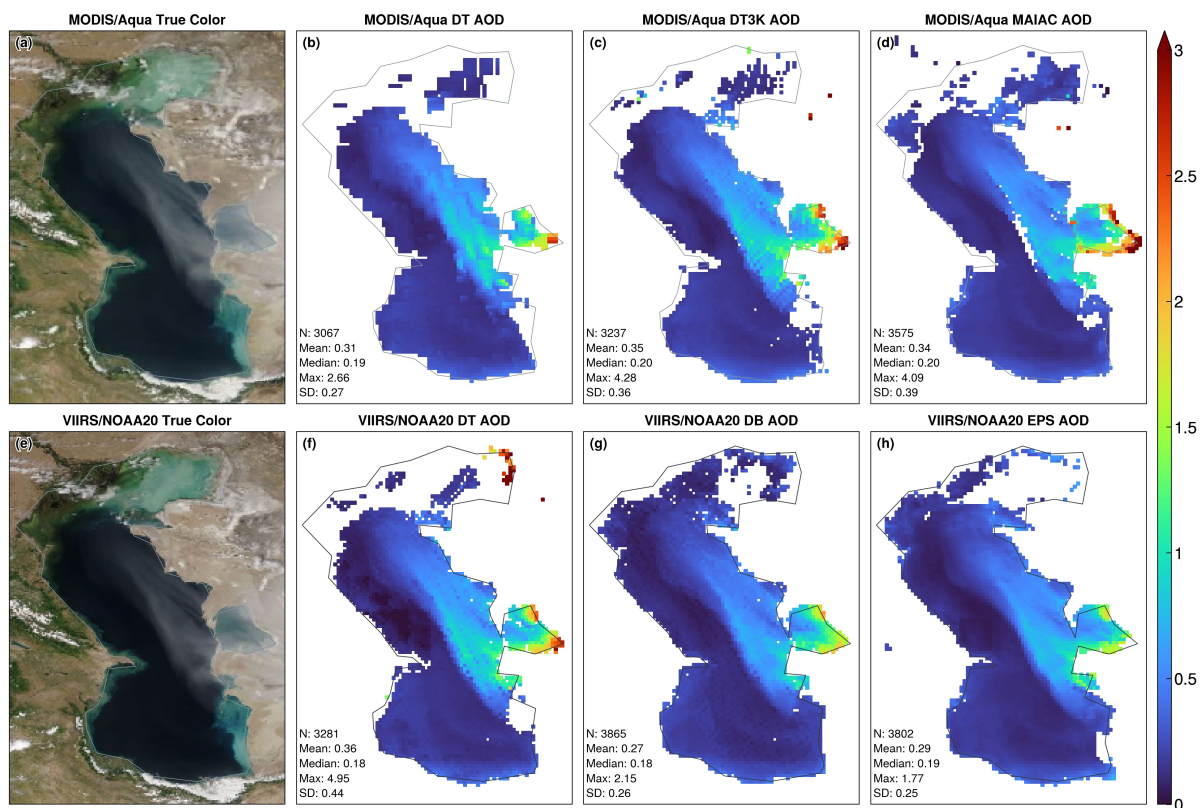


Figure 9. Multi-sensor AOD retrieval over the Caspian Sea on 28 May 2018. Top row panels are the MODIS/Aqua true color image (a), DT AOD (b), DT3K AOD (c), and MAIAC AOD (d). Bottom row panels are the VIIRS/NOAA20 true color image (e), DT AOD (f), DB AOD (g), and EPS AOD (h). All products are gridded to a $0.1^\circ \times 0.1^\circ$ resolution. The AOD summary statistics are shown on each panel.

the MAIAC product, which yields a greater number of pristine and heavily polluted pixels. The higher AOD limit in MAIAC (6 vs. 3.5 for DB) perhaps also contributes to a larger dynamic range and deviation from the DB product. For VIIRS, EPS generally yields lower AOD than DB under all conditions, with their difference increasing with the aerosol burden (Fig. 8b).
 495 For example, the EPS-DB difference increases from 37% when $AOD < 1$ to 51% when $4 < AOD < 5$. Indeed, Fig. 5 shows that EPS produces significantly lower AODs in dust-affected areas than other algorithms.

3.3.2 Dust outflow to Caspian Sea

Caspian Sea is affected by dust outflow from the adjacent deserts in Central Asia and distant sources in North Africa and the Middle East (Mohammadpour et al., 2022; Shukurov et al., 2023). As a source of micro-nutrients the dust outflow may
 500 contribute to intense algal blooms in the southern and southeastern parts of Caspian Sea where the marine productivity is limited by low nutrient levels (Modabberi et al., 2019; Kalinskaya et al., 2021). Fig. 9 displays the AOD retrieval over Caspian Sea on 28 May 2018, based on the best quality, over-water retrievals from MODIS (DT, DT3K, and MAIAC) and VIIRS (DT,



DB, and EPS). All six AOD products are regridded to a $0.1^\circ \times 0.1^\circ$ resolution. Bilinear interpolation is applied to the MODIS DT AOD to fill the data gaps due to reduced pixel resolutions at the swath edges. All products observed the elevated aerosol burden associated with dust outflow to the Garabogazköl gulf and eastern Caspian Sea. The three MODIS products show generally good agreement in the regional statistics. The VIIRS DT product show extremely large AOD over northern Caspian Sea, where the turbid water likely violates the “dark target” assumption in the over-water retrieval. The non-negligible water-leaving radiance from these pixels may be erroneously treated as aerosol signal, resulting in AOD overestimation compared to the VIIRS DB and EPS products.

The products are further compared via linear regression to examine the consistency between aerosol algorithms, as shown in Fig. 10. Compared to the over-land retrieval, the over-water retrievals show a better agreement in the AOD magnitude and strong linear correlations, with the R^2 above 0.9 and RMSD below 0.1 for all comparisons. In particular, the MODIS DT and DT3K products yield a slope of 0.98 and R^2 of 0.91, indicating excellent agreement. The linear model fits suggest that the DT algorithm yields smaller AOD under clean marine conditions (i.e. $AOD < 0.15$), and higher AOD over dust-affected areas compared to the MAIAC, DB, or EPS algorithms.

All over-water AOD algorithms assume a linear combination of one fine and one coarse mode in representing the ambient aerosol, and simultaneously retrieves the total AOD and FMF. Here we use the total AOD and FMF to compute the coarse-mode AOD from each product, which is then regridded to a $0.1^\circ \times 0.1^\circ$ resolution. The regridded coarse-mode AODs are compared via linear regression, as shown in Fig. 11. The coarse-mode AODs are strongly linearly correlated, but show larger inter-algorithm differences than the total AODs. In general, the DT algorithm tends to produce higher coarse-mode AOD under dust-laden conditions, compared to other algorithms.

3.4 Comparison of AOCHE products

Figure 12 displays several parameters from the EPIC AOCHE product on 28 and 29 May 2018, including the 680 nm surface reflectivity, 680 nm AOD, AOCHE, and AOCHE after applying a filter of $AOD > 1.8$. The heavy dust plume on 27 May 2018 was missed by EPIC and thus not shown. On 28 May 2018, the low surface reflectivity of Caspian Sea (i.e. below 0.03), combined with the elevated AOD (i.e. 0.5–1) associated with the dust outflow, provides a suitable condition for inferring AOCHE from the DOAS ratios in the oxygen A and B bands. Fig. 12e shows that the dust layer was elevated to an altitude of 1.5–2.5 km over the Caspian Sea, probably due to the orographic lifting by the Ustyurt Plateau.

Unlike the Caspian Sea, the surface reflectivity exceeds 0.18 over the desert surfaces surrounding the Aral Sea. Through radiative transfer simulations Xu et al. (2019) showed that the sensitivity of DOAS ratios to AOCHE started to diminish over bright surfaces, and that a high aerosol burden is needed to produce sufficiently strong aerosol signals for AOCHE to be retrievable from the DOAS measurements. Fig. 12 shows that on both days EPIC retrieved extremely large AODs (up to 6 at 680 nm) associated with the lofted dust over Turkmenistan and low AODs elsewhere. The retrieved AOCHE shows an opposite pattern, with low values over high aerosol burden areas and unrealistically high values over low aerosol burden areas. Therefore, we will employ the 680 nm AOD to filter the unreliable AOCHE retrieval associated with weak aerosol signals over desert areas.

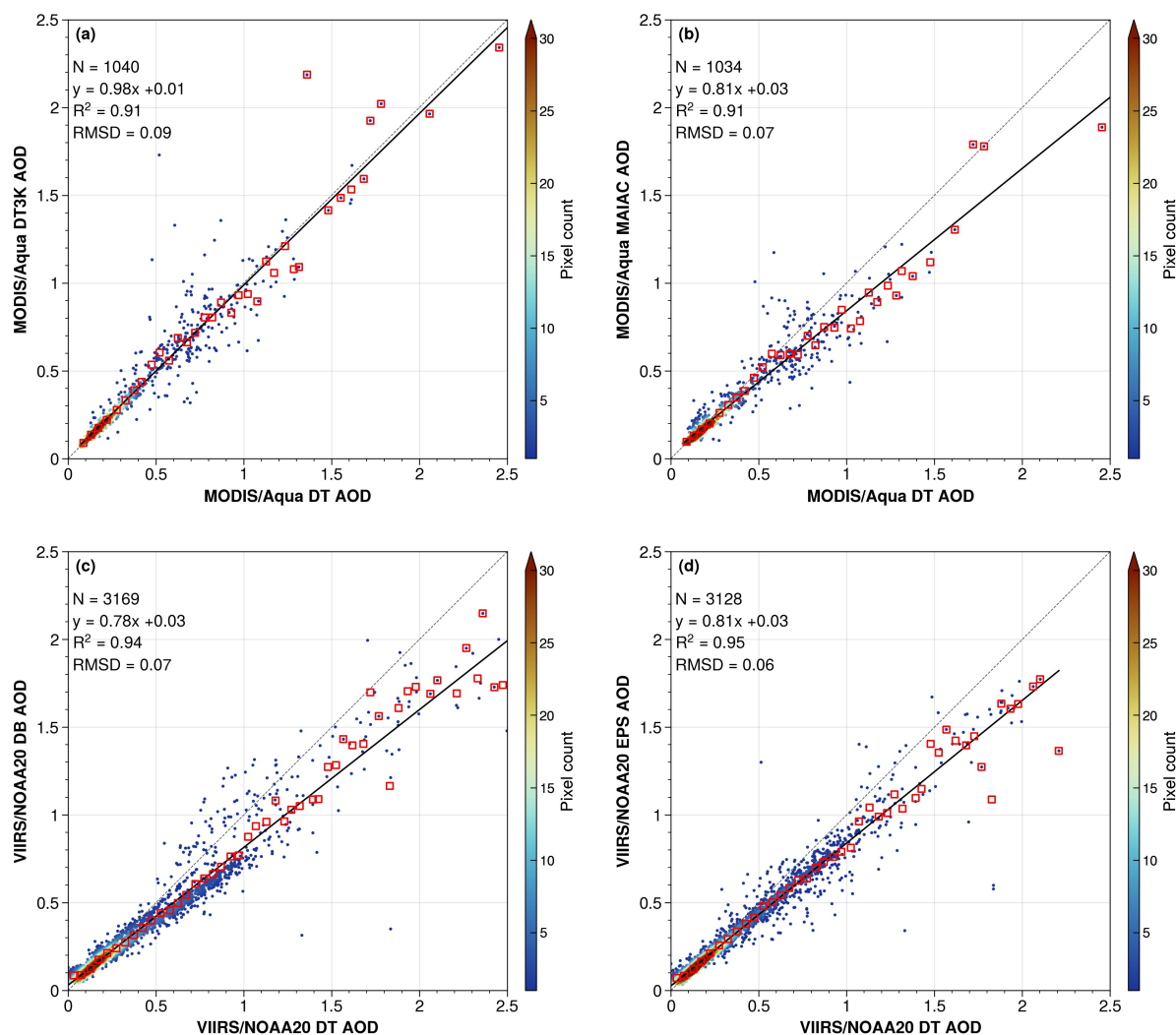


Figure 10. Comparison of AOD products using different algorithms over Caspian Sea on 28 May 2018: (a) MODIS/Aqua DT3K vs. DT; (b) MODIS/Aqua MAIAC vs. DT, (c) VIIRS/NOAA20 DB vs. DT, (d) VIIRS/NOAA20 EPS vs. DT. Black lines indicate the linear regression fits. Red squares indicate the bin-averaged AODs every 0.05 increments. RMSD, root mean square difference.

By applying a filter of $AOD > 1.8$, we find that the majority of the unrealistically high AOD pixels are removed, resulting in a spatially continuous AOD pattern from Turkmenistan to the Caspian Sea (Fig. 12g). The AOD-filtered AOD suggests that the lofted dust over Turkmenistan was located between 1–1.5 km on 28 May 2018, and between 2–3 km on 29 May 2018, or twice as high as the previous day. The temporal variation of dust height can be explained by the meteorological condition: a prevailing high pressure system may have suppressed the vertical aerosol mixing on 28 May 2018, whereas the enhanced upward vertical motion ahead of a deepening cold front promoted the convective mixing of the lofted dust on 29 May 2018.

540

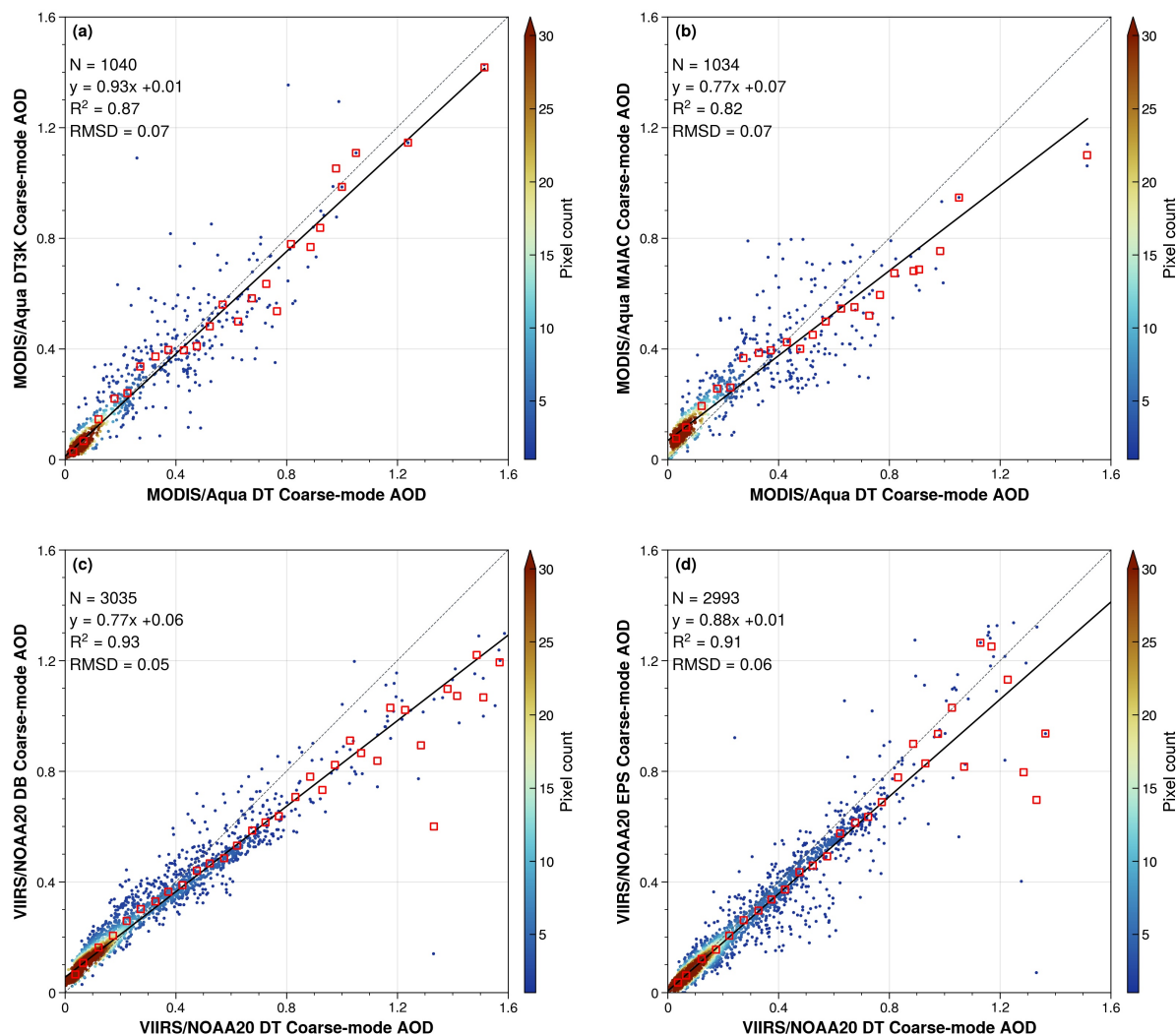


Figure 11. Same as Fig. 10 but for the coarse-mode AOD.

Using the daytime CALIOP overpass on 29 May 2018, we evaluated the accuracy of EPIC AOC_H against the CALIOP aerosol extinction-weight height, and explored the effects of wavelength choice (532 vs 1064 nm) and AOD filter. The CALIPSO ground track is shown in Fig. 12f. Past studies suggested that the CALIOP 1064 nm measurement is more sensitive to coarse aerosols close to the ground, while the 532 nm channel is subject to sensitivity loss in the presence of carbonaceous aerosols (Torres et al., 2013). Fig. 13a shows that the choice of 532 or 1064 nm has a minor effect on the CALIOP extinction-weighted height, with a mean difference below 0.1 km or 5%. Both indicate that the dust layer was mostly located between 1–2 km.

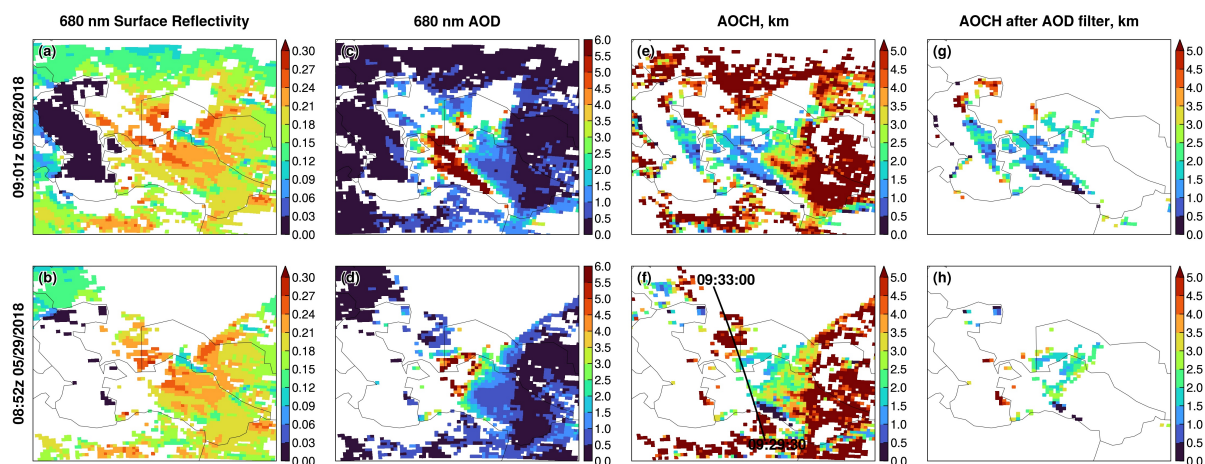


Figure 12. The 680 nm surface reflectivity (a, b), 680 nm AOD (c, d), AOC H (e, f), and AOC H after applying a filter of $AOD > 1.8$ (g, h) based on the EPIC AOC H product at 09:01z 28 May 2018 (top row) and 08:47z 29 May 2018 (bottom row). The daytime CALIPSO ground track on 29 May 2018 is shown in panel (f).

The EPIC AOC H has good agreement with CALIOP over the dusty or high AOD areas, but shows significant overestimation elsewhere. Using the CALIOP 532 nm extinction-weighted height as ground truth, Fig. 13b shows the mean bias and root-mean-square-error (RMSE) of the EPIC AOC H for a range of threshold AOD filters. EPIC persistently overestimates the aerosol height, especially under low aerosol burdens. The mean bias and RMSE are greatly improved and both fall below 0.5 km, when an AOD threshold of 1.8 or above is used to filter the EPIC AOC H. In other words, the EPIC AOC H product has the best agreement with CALIOP over regions affected by heavy dust burden (i.e. $AOD > 1.8$), where the mean bias and RMSE are comparable to the over-water AOC H retrieval as reported in previous studies (Xu et al., 2017, 2019). When using the 1064 measurement as ground truth, we find that the mean bias is slightly improved (0.25 vs. 0.3 km), while the RMSE is slightly degraded (0.58 vs. 0.42 km).

4 Conclusions

Driven by the desiccation of the Aral Sea, the newly formed Aralkum Desert has emerged as a major source of wind-blown saline dust aerosol in Central Asia. There is generally a poor understanding of the performance and consistency of satellite aerosol remote sensing techniques in observing the airborne dust from Aralkum Desert. This paper addresses this knowledge gap in two aspects.

First, we provided a review of the physical principles and algorithms used to retrieve UVAI, AOD, and AOC H over desert surfaces, focusing on the algorithms' treatment of regional aerosol optical properties and land surface reflectivity. As satellite remote sensing aerosol algorithms are generally optimized for global performance, the algorithm differences are expected to have a larger effect on the product performance and consistency over Central Asia, where the local aerosol and land surface

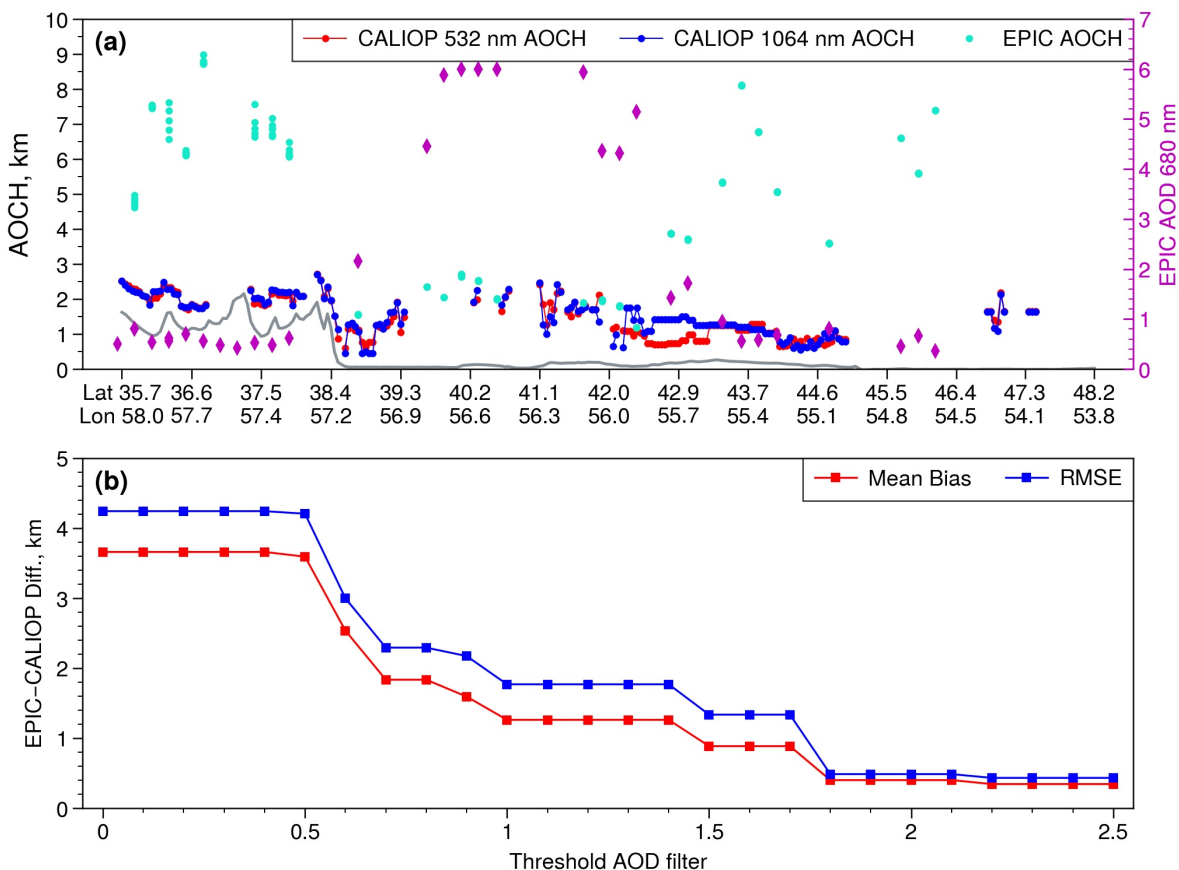


Figure 13. (a) Comparison between CALIOP 532 and 1064 nm aerosol extinction-weighted heights (dotted lines) and EPIC-retrieved ACH (cyan dots) along the CALIOP overpass on 29 May 2018 (ground track shown in Fig.12f). The EPIC-retrieved 680 nm AOD (magenta diamonds) and CALIOP-detected ground surface (gray line) are also shown. (b) The mean bias and RMSE of EPIC ACH against CALIOP 532 nm extinction-weighted height as a function of the threshold AOD used to filter the EPIC ACH retrieval.

conditions are under-represented in the aerosol algorithms. For example, the dust optical models used in the AOD and ACH algorithms are mostly derived from AERONET measurements over West Africa and the Middle East. The extent to which the dust optical models deviate from the saline dust from Aralkum (e.g., refractive index, size distribution) has yet to be determined.

570 The impact of the different algorithm assumptions on aerosol product performance in Central Asia is unknown.

Second, we presented a case analysis of the cross-sensor and cross-algorithm consistency in observing a saline dust storm from the Aralkum Desert during 27–29 May 2018. We considered a wide range of aerosol products, including the UVAI products from OMPS, TROPOMI, and EPIC, the AOD products from MODIS and VIIRS based on multiple algorithms (DT, DT3K, DB, MAIAC, and EPS), and the ACH derived from CALIOP aerosol extinction profile and EPIC oxygen absorption

575 spectroscopic measurements. The main findings are as follows.



The UVAI products show similar spatial patterns associated with the heavy dust plume on 27 May 2018, but reveal significant differences in magnitude and dynamic range. The differences can be explained, at least in part, by the choice of wavelength pair and the treatment of cloud scattering. Using the 95th percentile of each product as the threshold for dust detection, we find a general agreement between the products in delineating the areal extent of the dust plume. All UVAI products show large positive values over the northern Caspian Sea, Garabogazköl gulf, and Sor Kaydak salt marsh. This dust-like signal is primarily caused by enhanced UV absorption by turbid and saline waters, which causes the water-leaving UV radiances to deviate from a pure Rayleigh scattering atmosphere, similar to the effect of absorbing aerosols. Hence, caution must be used to avoid misinterpreting the surface effect as dust signal over ephemeral or dried water bodies, such as the Aralkum Desert.

The AOD products over desert surfaces are subject to significant inconsistency between different sensors and algorithms. The choice of aerosol algorithms causes a nonlinear response in the retrieved AOD from MODIS and VIIRS. Specifically, the MAIAC algorithm yields lower AOD than the DB algorithm under low aerosol burden, but higher AOD under heavy aerosol burden. The EPS algorithm yields lower AOD than DB under all aerosol burden conditions. The EPS-DB difference is found to increase with the aerosol burden. In addition, all AOD products erroneously classified the freshly emitted dust plume on 27 May 2018 as clouds. The EPS algorithm misused the urban aerosol optical model for dust retrieval, which may explain the significantly lower AOD in the VIIRS EPS product compared to other products.

There is generally good agreement between the over-water AOD retrievals in observing the dust outflow to the Caspian Sea. The AOD products show strong linear correlations and low RMSD, with the R^2 above 0.9 and RMSD below 0.1. We find that the DT algorithm tends to yield smaller AOD under clean marine conditions, but higher total and coarse-mode AOD under dust-laden conditions compared to the MAIAC, DB, and EPS algorithms.

Despite the high surface reflectivity which limits the passive AOC retrieval over Central Asia, we find that the EPIC AOC product retrieved the dust layer height reasonably, after applying an AOD filter to remove the unrealistic retrievals under low aerosol burdens. Specifically, the EPIC AOC product shows the best agreement with CALIOP aerosol extinction-weighted height over areas with $AOD > 1.8$, where both the mean bias and RMSE are below 0.5 km. However, the EPIC AOC product significantly overestimates the aerosol height over regions with low AOD burdens. The transported dust from Aralkum to Turkmenistan was located at an altitude of 1-1.5 km on 28 May 2018 due to a prevailing high pressure system, and lifted to an altitude of 2-3 km the next day, due to enhanced vertical mixing ahead of an advancing cold front. The dust outflow to the Caspian Sea was lifted to an altitude of 1.5-2.5 km, likely due to the orographic effect of the Ustyurt Plateau.

In summary, the dust event analysis allows us to conduct a detailed comparison of various satellite products in characterizing the airborne dust from the Aralkum Desert. The analysis reveals a potential limitation of using UVAI for dust detection and source mapping over Central Asia, due to the interference effect of turbid/salty waters, salt marshes, and saline deserts. While this study reveals substantial inconsistency between the AOD products, an extensive analysis (e.g., using multiple years' data) is needed to provide a more robust evaluation of the product differences in the retrieval fraction, climatological properties, and long-term trend. This study highlights the need for in situ measurements of the physiochemical and mineralogical properties of the saline dust from Aralkum, which are critical for improving the representation of the regional aerosol optical models used in satellite aerosol algorithms. We also call for routine ground-based aerosol measurements in the downwind region



(e.g., Karakalpakstan) to provide ground truth data for validating the satellite aerosol products. Finally, while the case study demonstrates the use of EPIC AOCHE product to quantify the dust layer height with a reasonable accuracy, an extensive analysis is desirable to evaluate the information content and skill of passive techniques in retrieving the aerosol vertical height over desert areas, particularly the role of surface reflectivity and aerosol optical properties.

615 *Data availability.* All the data used in the study are publicly available. The data repository links are provided in the reference column of Table 1. The regridded daily AOD products are available at <https://doi.org/10.5281/zenodo.13994593>.

Author contributions. XX designed the study and performed data curation, formal analysis, visualization, and writing of the initial draft. JW contributed to the writing of EPIC AOCHE algorithm. IL contributed to the writing of VIIRS EPS algorithm. CA and OT contributed to the UVAI analysis. AS, JL, RL, YW, AL, and IL contributed to AOD analysis. JW, ZL and OT contributed to the AOCHE analysis. All authors
620 edited the manuscript.

Competing interests. The authors declare no competing interests.

Acknowledgements. XX acknowledges support from the NASA Land-Cover and Land-Use Change (LCLUC) Program (grant no. 80NSSC20K1480). The satellite data teams acknowledge funding support from multiple NASA and NOAA funding sources supporting the multi-decadal development and evaluation of these data records. The authors gratefully acknowledge the Copernicus Data Space Ecosystem and NASA ASDC,
625 LAADS DAAC, and GES DISC for maintaining/distributing the data products used in this study.



References

- Abuduwaili, J., Liu, D. W., and Wu, G. Y.: Saline dust storms and their ecological impacts in arid regions, *Journal of Arid Land*, 2, 144–150, <https://doi.org/10.3724/SP.J.1227.2010.00144>, 2010.
- Argaman, E., Singer, A., and Tsoar, H.: Erodibility of some crust forming soils/sediments from the Southern Aral Sea Basin as determined in a wind tunnel, *Earth Surface Processes and Landforms*, 31, 47–63, <https://doi.org/10.1002/esp.1230>, 2006.
- ASDC: DSCOVR EPIC Aerosol Optical Centroid Height Version 1 [Dataset], https://doi.org/10.5067/EPIC/DSCOVR/L2_AOCH.001, 2018.
- ASDC: CALIPSO Lidar Level 2 Aerosol Profile, V4-51 [Data set], https://doi.org/10.5067/CALIOP/CALIPSO/CAL_LID_L2_05kmAPro-Standard-V4-51, 2023.
- Carr, J. L., Wu, D. L., Daniels, J., Friberg, M. D., Bresky, W., and Madani, H.: Geo-geo stereo-tracking of atmospheric motion vectors (AMVS) from the geostationary ring, *Remote Sensing*, 12, 1–47, <https://doi.org/10.3390/rs12223779>, 2020.
- Castellanos, P., Colarco, P., Espinosa, W. R., Guzewich, S. D., Levy, R. C., Miller, R. L., Chin, M., Kahn, R. A., Kempainen, O., Moosmüller, H., Nowotnick, E. P., Rocha-Lima, A., Smith, M. D., Yorks, J. E., and Yu, H.: Mineral dust optical properties for remote sensing and global modeling: A review, *Remote Sensing of Environment*, 303, <https://doi.org/10.1016/j.rse.2023.113982>, 2024.
- Chen, X., Wang, J., Xu, X., Zhou, M., Zhang, H., Castro Garcia, L., Colarco, P. R., Janz, S. J., Yorks, J., McGill, M., Reid, J. S., de Graaf, M., and Kondragunta, S.: First retrieval of absorbing aerosol height over dark target using TROPOMI oxygen B band: Algorithm development and application for surface particulate matter estimates, *Remote Sensing of Environment*, 265, <https://doi.org/10.1016/j.rse.2021.112674>, 2021.
- de Graaf, M., Stammes, P., Torres, O., and Koелеmeijer, R. B.: Absorbing Aerosol Index: Sensitivity analysis, application to GOME and comparison with TOMS, *Journal of Geophysical Research D: Atmospheres*, 110, 1–19, <https://doi.org/10.1029/2004JD005178>, 2005.
- Di Biagio, C., Formenti, P., Balkanski, Y., Caponi, L., Cazaunau, M., Pangui, E., Journet, E., Nowak, S., Andreae, M. O., Kandler, K., Saeed, T., Piketh, S., Seibert, D., Williams, E., and Doussin, J. F.: Complex refractive indices and single-scattering albedo of global dust aerosols in the shortwave spectrum and relationship to size and iron content, *Atmospheric Chemistry and Physics*, 19, 15 503–15 531, <https://doi.org/10.5194/acp-19-15503-2019>, 2019.
- Ding, S., Wang, J., and Xu, X.: Polarimetric remote sensing in oxygen A and B bands: Sensitivity study and information content analysis for vertical profile of aerosols, *Atmospheric Measurement Techniques*, 9, 2077–2092, <https://doi.org/10.5194/amt-9-2077-2016>, 2016.
- Dubovik, O., Holben, B., Eck, T. F., Smirnov, A., Kaufman, Y. J., King, M. D., Tanré, D., and Slutsker, I.: Variability of Absorption and Optical Properties of Key Aerosol Types Observed in Worldwide Locations, *Journal of the Atmospheric Sciences*, 59, 590–608, [https://doi.org/10.1175/1520-0469\(2002\)059<0590:voaaop>2.0.co;2](https://doi.org/10.1175/1520-0469(2002)059<0590:voaaop>2.0.co;2), 2002.
- Dubovik, O., Sinyuk, A., Lapyonok, T., Holben, B. N., Mishchenko, M., Yang, P., Eck, T. F., Volten, H., Muñoz, O., Veihelmann, B., van der Zande, W. J., Leon, J. F., Sorokin, M., and Slutsker, I.: Application of spheroid models to account for aerosol particle nonsphericity in remote sensing of desert dust, *Journal of Geophysical Research Atmospheres*, 111, <https://doi.org/10.1029/2005JD006619>, 2006.
- ESA: TROPOMI Level 2 Ultraviolet Aerosol Index products Version 02 [Data set], <https://doi.org/10.5270/S5P-3dgz66p>, 2021.
- Groll, M., Opp, C., and Aslanov, I.: Spatial and temporal distribution of the dust deposition in central asia - results from a long term monitoring program, *Aeolian Research*, 9, 49–62, <https://doi.org/10.1016/j.aeolia.2012.08.002>, 2013.
- Groll, M., Opp, C., Issanova, G., Vereshagina, N., and Semenov, O.: Physical and chemical characterization of dust deposited in the Turan Lowland (Central Asia), in: *E3S Web of Conferences*, vol. 99, ISSN 22671242, <https://doi.org/10.1051/e3sconf/20199903005>, 2019.



- He, X., Bai, Y., Pan, D., Tang, J., and Wang, D.: Atmospheric correction of satellite ocean color imagery using the ultraviolet wavelength for highly turbid waters, *Optics Express*, 20, 20 754, <https://doi.org/10.1364/oe.20.020754>, 2012.
- Herman, J. R. and Celarier, E. A.: Earth surface reflectivity climatology at 340-380 nm from TOMS data, *Journal of Geophysical Research Atmospheres*, 102, 28 003–28 011, <https://doi.org/10.1029/97jd02074>, 1997.
- 665 Herman, J. R., Bhartia, P. K., Torres, O., Hsu, C., Seftor, C., and Celarier, E.: Global distribution of UV-absorbing aerosols from Nimbus 7/TOMS data, *Journal of Geophysical Research Atmospheres*, 102, 16 911–16 922, <https://doi.org/10.1029/96jd03680>, 1997.
- Holben, B. N., Eck, T. F., Slutsker, I., Tanré, D., Buis, J. P., Setzer, A., Vermote, E., Reagan, J. A., Kaufman, Y. J., Nakajima, T., Lavenu, F., Jankowiak, I., and Smirnov, A.: AERONET - A federated instrument network and data archive for aerosol characterization, *Remote Sensing of Environment*, 66, 1–16, [https://doi.org/10.1016/S0034-4257\(98\)00031-5](https://doi.org/10.1016/S0034-4257(98)00031-5), 1998.
- 670 Hsu, C.: VIIRS/NOAA20 Deep Blue Aerosol L2 6-Min Swath 6 km [Data set], https://doi.org/doi.org/10.5067/VIIRS/AERDB_L2_VIIRS_NOAA20.002.2022.
- Hsu, N. C.: Detection of biomass burning smoke from TOMS measurements, <https://doi.org/10.1029/96GL00455>, 1996.
- Hsu, N. C., Tsay, S. C., King, M. D., and Herman, J. R.: Aerosol properties over bright-reflecting source regions, *IEEE Transactions on Geoscience and Remote Sensing*, 42, 557–569, <https://doi.org/10.1109/TGRS.2004.824067>, 2004.
- 675 Hsu, N. C., Jeong, M. J., Bettenhausen, C., Sayer, A. M., Hansell, R., Seftor, C. S., Huang, J., and Tsay, S. C.: Enhanced Deep Blue aerosol retrieval algorithm: The second generation, *Journal of Geophysical Research Atmospheres*, 118, 9296–9315, <https://doi.org/10.1002/jgrd.50712>, 2013.
- Hsu, N. C., Lee, J., Sayer, A. M., Kim, W., Bettenhausen, C., and Tsay, S. C.: VIIRS Deep Blue Aerosol Products Over Land: Extending the EOS Long-Term Aerosol Data Records, *Journal of Geophysical Research: Atmospheres*, 124, 4026–4053, <https://doi.org/10.1029/2018JD029688>, 2019.
- 680 Indoitu, R., Kozhoridze, G., Batyrbaeva, M., Vitkovskaya, I., Orlovsky, N., Blumberg, D., and Orlovsky, L.: Dust emission and environmental changes in the dried bottom of the Aral Sea, *Aeolian Research*, 17, 101–115, <https://doi.org/10.1016/j.aeolia.2015.02.004>, 2015.
- Jackson, J. M., Liu, H., Laszlo, I., Kondragunta, S., Remer, L. A., Huang, J., and Huang, H. C.: Suomi-NPP VIIRS aerosol algorithms and data products, *Journal of Geophysical Research Atmospheres*, 118, 673–12, <https://doi.org/10.1002/2013JD020449>, 2013.
- 685 Jiang, H., Huang, J., Li, L., Huang, L., Manzoor, M., Yang, J., Wu, G., Sun, X., Wang, B., Egamberdieva, D., Panosyan, H., Birkeland, N. K., Zhu, Z., and Li, W.: Onshore soil microbes and endophytes respond differently to geochemical and mineralogical changes in the Aral Sea, *Science of the Total Environment*, 765, <https://doi.org/10.1016/j.scitotenv.2020.142675>, 2021.
- Kalinskaya, D. V., Medvedeva, A. V., and Aleskerova, A. A.: The Influence of Dust Transport on the Intensity of Cyanobacterial Bloom in the Caspian Sea, *Atmospheric and Oceanic Optics*, 34, 611–616, <https://doi.org/10.1134/S1024856021060154>, 2021.
- 690 Kaufman, Y. J., Tanré, D., Remer, L. A., Vermote, E. F., Chu, A., and Holben, B. N.: Operational remote sensing of tropospheric aerosol over land from EOS moderate resolution imaging spectroradiometer, *Journal of Geophysical Research Atmospheres*, 102, 17 051–17 067, <https://doi.org/10.1029/96jd03988>, 1997a.
- Kaufman, Y. J., Wald, A. E., Remer, L. A., Gao, B. C., Li, R. R., and Flynn, L.: MODIS 2.1- μm channel - correlation with visible reflectance for use in remote sensing of aerosol, *IEEE Transactions on Geoscience and Remote Sensing*, 35, 1286–1298, <https://doi.org/10.1109/36.628795>, 1997b.
- 695 Kim, M. H., Omar, A. H., Tackett, J. L., Vaughan, M. A., Winker, D. M., Trepte, C. R., Hu, Y., Liu, Z., Poole, L. R., Pitts, M. C., Kar, J., and Magill, B. E.: The CALIPSO version 4 automated aerosol classification and lidar ratio selection algorithm, *Atmospheric Measurement Techniques*, 11, 6107–6135, <https://doi.org/10.5194/amt-11-6107-2018>, 2018.



- 700 Koffi, B., Schulz, M., Bréon, F. M., Griesfeller, J., Winker, D., Balkanski, Y., Bauer, S., Berntsen, T., Chin, M., Collins, W. D., Dentener, F., Diehl, T., Easter, R., Ghan, S., Ginoux, P., Gong, S., Horowitz, L. W., Iversen, T., Kirkevg, A., Koch, D., Krol, M., Myhre, G., Stier, P., and Takemura, T.: Application of the CALIOP layer product to evaluate the vertical distribution of aerosols estimated by global models: AeroCom phase i results, <https://doi.org/10.1029/2011JD016858>, 2012.
- Kokhanovsky, A. A., Davis, A. B., Cairns, B., Dubovik, O., Hasekamp, O. P., Sano, I., Mukai, S., Rozanov, V. V., Litvinov, P., Lapyonok, T., Kolomiets, I. S., Oberemok, Y. A., Savenkov, S., Martin, W., Wasilewski, A., Di Noia, A., Stap, F. A., Rietjens, J., Xu, F., Natraj, V., Duan, M., Cheng, T., and Munro, R.: Space-based remote sensing of atmospheric aerosols: The multi-angle spectro-polarimetric frontier, <https://doi.org/10.1016/j.earscirev.2015.01.012>, 2015.
- Kondragunta, S., Laszlo, I., and Ma, L.: NOAA JPSS Visible Infrared Imaging Radiometer Suite (VIIRS) Aerosol Optical Depth and Aerosol Particle Size Distribution Environmental Data Record (EDR) from NDE, <https://doi.org/10.7289/V5319T4H>, 2023.
- 710 Laszlo, I.: Remote Sensing of Tropospheric Aerosol Optical Depth From Multispectral Monodirectional Space-Based Observations, in: *Comprehensive Remote Sensing*, edited by Liang, S. B. T. C. R. S., pp. 137–196, Elsevier, Oxford, ISBN 978-0-12-803221-3, <https://doi.org/https://doi.org/10.1016/B978-0-12-409548-9.10389-6>, 2018.
- Laszlo, I. and Liu, H.: EPS Aerosol Optical Depth (AOD) Algorithm Theoretical Basis Document Version 3.4, Tech. rep., NOAA NESDIS CENTER for SATELLITE APPLICATIONS and RESEARCH, https://www.star.nesdis.noaa.gov/jps/documents/ATBD/ATBD_EPS_Aerosol_AOD_v3.4.pdf, 2022.
- 715 Lee, J., Hsu, N. C., Sayer, A. M., Bettenhausen, C., and Yang, P.: AERONET-Based Nonspherical Dust Optical Models and Effects on the VIIRS Deep Blue/SOAR Over Water Aerosol Product, *Journal of Geophysical Research: Atmospheres*, 122, 10 384–10 401, <https://doi.org/10.1002/2017JD027258>, 2017.
- Lee, J., Hsu, N. C., Kim, W. V., Sayer, A. M., and Tsay, S.-C.: VIIRS Version 2 Deep Blue Aerosol Products, *Journal of Geophysical Research: Atmospheres*, 129, e2023JD040 082, <https://doi.org/https://doi.org/10.1029/2023JD040082>, 2024.
- 720 Lee, Z., Hu, C., Shang, S., Du, K., Lewis, M., Arnone, R., and Brewin, R.: Penetration of UV-visible solar radiation in the global oceans: Insights from ocean color remote sensing, *Journal of Geophysical Research: Oceans*, 118, 4241–4255, <https://doi.org/10.1002/jgrc.20308>, 2013.
- Levy, R. C. and Hsu, N. C.: MODIS Atmosphere L2 Aerosol Product [Data set], https://doi.org/10.5067/MODIS/MYD04_L2.006, 2015a.
- 725 Levy, R. C. and Hsu, N. C.: MODIS Atmosphere L2 Aerosol Product [Dataset], https://doi.org/10.5067/MODIS/MOD04_3K.061, 2015b.
- Levy, R. C., Remer, L. A., and Dubovik, O.: Global aerosol optical properties and application to Moderate Resolution Imaging Spectroradiometer aerosol retrieval over land, *Journal of Geophysical Research Atmospheres*, 112, <https://doi.org/10.1029/2006JD007815>, 2007.
- Levy, R. C., Mattoo, S., Munchak, L. A., Remer, L. A., Sayer, A. M., Patadia, F., and Hsu, N. C.: The Collection 6 MODIS aerosol products over land and ocean, *Atmospheric Measurement Techniques*, 6, 2989–3034, <https://doi.org/10.5194/amt-6-2989-2013>, 2013.
- 730 Levy, R. C., Mattoo, S., Sawyer, V., and Munchak, L.: VIIRS/NOAA20 Dark Target Aerosol 6-Min L2 Swath 6 km [Dataset], https://doi.org/10.5067/VIIRS/AERDT_L2_VIIRS_NOAA20.002, 2023.
- Li, J., Carlson, B. E., and Laci, A. A.: How well do satellite AOD observations represent the spatial and temporal variability of PM_{2.5} concentration for the United States?, *Atmospheric Environment*, 102, 260–273, <https://doi.org/10.1016/j.atmosenv.2014.12.010>, 2015.
- 735 Lu, Z., Wang, J., Xu, X., Chen, X., Kondragunta, S., Torres, O., Wilcox, E. M., and Zeng, J.: Hourly Mapping of the Layer Height of Thick Smoke Plumes Over the Western U.S. in 2020 Severe Fire Season, *Frontiers in Remote Sensing*, 2, <https://doi.org/10.3389/frsen.2021.766628>, 2021.



- Lu, Z., Wang, J., Chen, X., Zeng, J., Wang, Y., Xu, X., Christian, K. E., Yorks, J. E., Nowotnick, E. P., Reid, J. S., and Xian, P.: First Mapping of Monthly and Diurnal Climatology of Saharan Dust Layer Height Over the Atlantic Ocean From EPIC/DSCOVR in Deep Space, *Geophysical Research Letters*, 50, <https://doi.org/10.1029/2022GL102552>, 2023.
- 740 Lyapustin, A. and Wang, Y.: MODIS/Terra+Aqua Land Aerosol Optical Depth Daily L2G Global 1km SIN Grid V061 [Data set], <https://doi.org/10.5067/MODIS/MCD19A2.061>, 2022.
- Lyapustin, A., Wang, Y., Korkin, S., and Huang, D.: MODIS Collection 6 MAIAC algorithm, *Atmospheric Measurement Techniques*, 11, 5741–5765, <https://doi.org/10.5194/amt-11-5741-2018>, 2018.
- Lyapustin, A., Wang, Y., Korkin, S., Kahn, R., and Winker, D.: MAIAC Thermal Technique for Smoke Injection Height from MODIS, *IEEE Geoscience and Remote Sensing Letters*, 17, 730–734, <https://doi.org/10.1109/LGRS.2019.2936332>, 2020.
- 745 Marshak, A., Herman, J., Szabo, A., Blank, K., Carn, S., Cede, A., Geogdzhayev, I., Huang, D., Huang, L. K., Knyazikhin, Y., Kowalewski, M., Krotkov, N., Lyapustin, A., McPeters, R., Meyer, K. G., Torres, O., and Yang, Y.: Earth observations from DSCOVR epic instrument, *Bulletin of the American Meteorological Society*, 99, 1829–1850, <https://doi.org/10.1175/BAMS-D-17-0223.1>, 2018.
- Modabberi, A., Noori, R., Madani, K., Ehsani, A. H., Danandeh Mehr, A., Hooshyaripor, F., and Kløve, B.: Caspian Sea is eutrophying: The alarming message of satellite data, *Environmental Research Letters*, 15, <https://doi.org/10.1088/1748-9326/abc6d3>, 2019.
- 750 Mohammadpour, K., Sciortino, M., Kaskaoutis, D. G., and Rashki, A.: Classification of synoptic weather clusters associated with dust accumulation over southeastern areas of the Caspian Sea (Northeast Iran and Karakum desert), *Aeolian Research*, 54, <https://doi.org/10.1016/j.aeolia.2022.100771>, 2022.
- Moradi, M.: Interannual and intra-annual cycles of satellite-derived chlorophyll-a concentrations in the Caspian Sea, *Journal of Great Lakes Research*, 48, 143–158, <https://doi.org/10.1016/j.jglr.2021.10.021>, 2022.
- 755 Munchak, L. A., Levy, R. C., Mattoo, S., Remer, L. A., Holben, B. N., Schafer, J. S., Hostetler, C. A., and Ferrare, R. A.: MODIS 3 km aerosol product: Applications over land in an urban/suburban region, *Atmospheric Measurement Techniques*, 6, 1747–1759, <https://doi.org/10.5194/amt-6-1747-2013>, 2013.
- Nelson, D. L., Garay, M. J., Kahn, R. A., and Dunst, B. A.: Stereoscopic height and wind retrievals for aerosol plumes with the MISR Interactive eXplorer (MINX), *Remote Sensing*, 5, 4593–4628, <https://doi.org/10.3390/rs5094593>, 2013.
- 760 Nobakht, M., Shahgedanova, M., and White, K.: New Inventory of Dust Emission Sources in Central Asia and Northwestern China Derived From MODIS Imagery Using Dust Enhancement Technique, *Journal of Geophysical Research: Atmospheres*, 126, <https://doi.org/10.1029/2020JD033382>, 2021.
- Omar, A. H., Winker, D. M., Kittaka, C., Vaughan, M. A., Liu, Z., Hu, Y., Trepte, C. R., Rogers, R. R., Ferrare, R. A., Lee, K. P., Kuehn, R. E., and Hostetler, C. A.: The CALIPSO automated aerosol classification and lidar ratio selection algorithm, *Journal of Atmospheric and Oceanic Technology*, 26, 1994–2014, <https://doi.org/10.1175/2009JTECHA1231.1>, 2009.
- 765 Orlovsky, L. and Orlovsky, N.: White sand storms in Central Asia, in: *Global Alarm: Dust and Sand Storms from the World's Dry lands*, edited by Yang, Y., Squires, V., and Lu, Q., chap. 8, pp. 169–201, United Nations, 2001.
- Peyridieu, S., Chédin, A., Tanré, D., Capelle, V., Pierangelo, C., Lamquin, N., and Armante, R.: Saharan dust infrared optical depth and altitude retrieved from AIRS: A focus over North Atlantic-comparison to MODIS and CALIPSO, *Atmospheric Chemistry and Physics*, 10, 1953–1967, <https://doi.org/10.5194/acp-10-1953-2010>, 2010.
- 770 Pierangelo, C., Chédin, A., Heilliette, S., Jacquinet-Husson, N., and Armante, R.: Dust altitude and infrared optical depth from AIRS, *Atmospheric Chemistry and Physics*, 4, 1813–1822, <https://doi.org/10.5194/acp-4-1813-2004>, 2004.



- Prospero, J. M., Ginoux, P., Torres, O., Nicholson, S. E., and Gill, T. E.: Environmental characterization of global sources of atmospheric
775 soil dust identified with the Nimbus 7 Total Ozone Mapping Spectrometer (TOMS) absorbing aerosol product, *Reviews of Geophysics*,
40, 2–1, <https://doi.org/10.1029/2000RG000095>, 2002.
- Radio Free Europe Radio Liberty: It's Raining Salt: Toxic Aral Sea Storm Sparks Health Fears In Central Asia, <https://www.rferl.org/a/toxic-aral-sea-salt-storm-sweeps-over-parts-of-uzbekistan-turkmenistan/29257503.html>, 2018.
- Remer, L. A., Kaufman, Y. J., Tanré, D., Mattoo, S., Chu, D. A., Martins, J. V., Li, R. R., Ichoku, C., Levy, R. C., Kleidman, R. G., Eck,
780 T. F., Vermote, E., and Holben, B. N.: The MODIS aerosol algorithm, products, and validation, *Journal of the Atmospheric Sciences*, 62,
947–973, <https://doi.org/10.1175/JAS3385.1>, 2005.
- Remer, L. A., Didier, T. ., Kaufman, Y. J., Levy, R., and Mattoo, S.: Algorithm for remote sensing of tropospheric aerosol from MODIS:
Collection 5 ATBD, Tech. rep., NASA, Greenbelt, MD, 2006.
- Remer, L. A., Brogniez, C., Cairns, B., Hsu, N. C., Kahn, R., Stammes, P., Tanré, D., and Torres, O.: Recent instruments and algorithms
785 for passive shortwave remote sensing, in: *Aerosol Remote Sensing*, edited by Lenoble, J., Remer, L., and Tanre, D., vol. 9783642177,
pp. 185–222, Springer Berlin Heidelberg, Berlin, Heidelberg, ISBN 978-3-642-17725-5, https://doi.org/10.1007/978-3-642-17725-5_8,
2013a.
- Remer, L. A., Mattoo, S., Levy, R. C., and Munchak, L. A.: MODIS 3 km aerosol product: Algorithm and global perspective, *Atmospheric
Measurement Techniques*, 6, 1829–1844, <https://doi.org/10.5194/amt-6-1829-2013>, 2013b.
- 790 Rudich, Y., Khersonsky, O., and Rosenfeld, D.: Treating clouds with a grain of salt, *Geophysical Research Letters*, 29, 17–1,
<https://doi.org/10.1029/2002gl016055>, 2002.
- Rupakheti, D., Rupakheti, M., Abdullaev, S. F., Yin, X., and Kang, S.: Columnar aerosol properties and radiative effects over Dushanbe,
Tajikistan in Central Asia, *Environmental Pollution*, 265, <https://doi.org/10.1016/j.envpol.2020.114872>, 2020.
- Samset, B. H., Stjern, C. W., Andrews, E., Kahn, R. A., Myhre, G., Schulz, M., and Schuster, G. L.: Aerosol Absorption: Progress Towards
795 Global and Regional Constraints, <https://doi.org/10.1007/s40641-018-0091-4>, 2018.
- Sawyer, V., Levy, R. C., Mattoo, S., Cureton, G., Shi, Y., and Remer, L. A.: Continuing the MODIS dark target aerosol time series with
VIIRS, *Remote Sensing*, 12, <https://doi.org/10.3390/rs12020308>, 2020.
- Sayer, A. M., Hsu, N. C., Lee, J., Bettenhausen, C., Kim, W. V., and Smirnov, A.: Satellite Ocean Aerosol Retrieval (SOAR) Algorithm
Extension to S-NPP VIIRS as Part of the “Deep Blue” Aerosol Project, *Journal of Geophysical Research: Atmospheres*, 123, 380–400,
800 <https://doi.org/10.1002/2017JD027412>, 2018.
- Schepanski, K., Tegen, I., and Macke, A.: Comparison of satellite based observations of Saharan dust source areas, *Remote Sensing of
Environment*, 123, 90–97, <https://doi.org/10.1016/j.rse.2012.03.019>, 2012.
- Shukurov, K. A., Simonenkov, D. V., Nevzorov, A. V., Rashki, A., Hamzeh, N. H., Abdullaev, S. F., Shukurova, L. M., and Chkhetiani, O. G.:
CALIOP-Based Evaluation of Dust Emissions and Long-Range Transport of the Dust from the Aral-Caspian Arid Region by 3D-Source
805 Potential Impact (3D-SPI) Method, *Remote Sensing*, 15, <https://doi.org/10.3390/rs15112819>, 2023.
- Singer, A., Banin, A., Poberezsky, L., and Gilenko, M.: Soil Crusts in the Amudarya River Delta: Properties and Formation, in: *Sustainable
Land Use in Deserts*, edited by Breckle, S.-W., Veste, M., and Wucherer, W., pp. 103–114, Springer Berlin Heidelberg, Berlin, Heidelberg,
ISBN 978-3-642-59560-8, https://doi.org/10.1007/978-3-642-59560-8_10, 2001.
- Singer, A., Zobeck, T., Poberezsky, L., and Argaman, E.: The PM10 and PM2.5 dust generation potential of soils/sediments in the Southern
810 Aral Sea Basin, Uzbekistan, *Journal of Arid Environments*, 54, 705–728, <https://doi.org/10.1006/jare.2002.1084>, 2003.



- Sokolik, I. N. and Toon, O. B.: Incorporation of mineralogical composition into models of the radiative properties of mineral aerosol from UV to IR wavelengths, *Journal of Geophysical Research Atmospheres*, 104, 9423–9444, <https://doi.org/10.1029/1998JD200048>, 1999.
- Stein Zweers, D. C.: TROPOMI ATBD of the UV aerosol index document number - S5P-KNMI-L2-0008-RP, Tech. Rep. 2.1.0, Royal Netherlands Meteorological Institute, De Bilt, 3731 GA, the Netherlands, <https://sentinel.esa.int/documents/247904/2476257/Sentinel-5P-TROPOMI-ATBD-UV-Aerosol-Index.pdf>, 2022.
- 815 Sun, J., Veefkind, P., Nanda, S., Van Velthoven, P., and Levelt, P.: The role of aerosol layer height in quantifying aerosol absorption from ultraviolet satellite observations, *Atmospheric Measurement Techniques*, 12, 6319–6340, <https://doi.org/10.5194/amt-12-6319-2019>, 2019.
- Tanré, D., Kaufman, Y. J., Herman, M., and Mattoo, S.: Remote sensing of aerosol properties over oceans using the MODIS/EOS spectral radiances, *Journal of Geophysical Research Atmospheres*, 102, 16 971–16 988, <https://doi.org/10.1029/96jd03437>, 1997.
- 820 Torres, O.: OMI/Aura Near UV Aerosol Optical Depth and Single Scattering Albedo 1-orbit L2 Swath 13x24 km V003 [Data set], <https://doi.org/10.5067/Aura/OMI/DATA2004>, 2006.
- Torres, O.: OMPS-NPP L2 NM Aerosol Index swath orbital V2 [Data set], <https://doi.org/10.5067/40L92G8144IV>, 2019a.
- Torres, O.: DSCOVR EPIC Level 2 UV Aerosol Version 3 [Data set], https://doi.org/10.5067/EPIC/DSCOVR/L2_AER_03, 2019b.
- Torres, O.: TROPOMI/Sentinel-5P Near UV Aerosol Optical Depth and Single Scattering Albedo L2 1-Orbit Snapshot 7.5 km x 3 km [Data set], <https://doi.org/10.5067/MEASURES/AER/DATA204>, 2021.
- 825 Torres, O., Bhartia, P. K., Herman, J. R., Ahmad, Z., and Gleason, J.: Derivation of aerosol properties from satellite measurements of backscattered ultraviolet radiation: Theoretical basis, *Journal of Geophysical Research Atmospheres*, 103, 17 099–17 110, <https://doi.org/10.1029/98JD00900>, 1998.
- Torres, O., Jethva, H., and Bhartia, P. K.: Retrieval of aerosol optical depth above clouds from OMI observations: Sensitivity analysis and case studies, *Journal of the Atmospheric Sciences*, 69, 1037–1053, <https://doi.org/10.1175/JAS-D-11-0130.1>, 2012.
- 830 Torres, O., Ahn, C., and Chen, Z.: Improvements to the OMI near-UV aerosol algorithm using A-train CALIOP and AIRS observations, *Atmospheric Measurement Techniques*, 6, 3257–3270, <https://doi.org/10.5194/amt-6-3257-2013>, 2013.
- Torres, O., Bhartia, P. K., Jethva, H., and Ahn, C.: Impact of the ozone monitoring instrument row anomaly on the long-term record of aerosol products, *Atmospheric Measurement Techniques*, 11, 2701–2715, <https://doi.org/10.5194/amt-11-2701-2018>, 2018.
- 835 Veefkind, J. P., Aben, I., McMullan, K., Förster, H., de Vries, J., Otter, G., Claas, J., Eskes, H. J., de Haan, J. F., Kleipool, Q., van Weele, M., Hasekamp, O., Hoogeveen, R., Landgraf, J., Snel, R., Tol, P., Ingmann, P., Voors, R., Kruizinga, B., Vink, R., Visser, H., and Levelt, P. F.: TROPOMI on the ESA Sentinel-5 Precursor: A GMES mission for global observations of the atmospheric composition for climate, air quality and ozone layer applications, *Remote Sensing of Environment*, 120, 70–83, <https://doi.org/10.1016/j.rse.2011.09.027>, 2012.
- Winker, D. M., Vaughan, M. A., Omar, A., Hu, Y., Powell, K. A., Liu, Z., Hunt, W. H., and Young, S. A.: Overview of the CALIPSO mission and CALIOP data processing algorithms, *Journal of Atmospheric and Oceanic Technology*, 26, 2310–2323, <https://doi.org/10.1175/2009JTECHA1281.1>, 2009.
- 840 Wu, L., Hasekamp, O., van Diedenhoven, B., Cairns, B., Yorks, J. E., and Chowdhary, J.: Passive remote sensing of aerosol layer height using near-UV multiangle polarization measurements, *Geophysical Research Letters*, 43, 8783–8790, <https://doi.org/10.1002/2016GL069848>, 2016.
- 845 Xi, X.: On the Geomorphic, Meteorological, and Hydroclimatic Drivers of the Unusual 2018 Early Summer Salt Dust Storms in Central Asia, *Journal of Geophysical Research: Atmospheres*, 128, <https://doi.org/10.1029/2022JD038089>, 2023.
- Xi, X. and Sokolik, I. N.: Seasonal dynamics of threshold friction velocity and dust emission in Central Asia, *Journal of Geophysical Research: Atmospheres*, 120, 1536–1564, <https://doi.org/10.1002/2014JD022471>, 2015a.



- 850 Xi, X. and Sokolik, I. N.: Dust interannual variability and trend in Central Asia from 2000 to 2014 and their climatic linkages, *Journal of Geophysical Research: Atmospheres*, 120, 12 175–12 197, <https://doi.org/10.1002/2015JD024092>, 2015b.
- Xi, X. and Sokolik, I. N.: Quantifying the anthropogenic dust emission from agricultural land use and desiccation of the Aral Sea in Central Asia, *Journal of Geophysical Research: Atmospheres*, 121, 270–12, <https://doi.org/10.1002/2016JD025556>, 2016.
- 855 Xu, X., Wang, J., Wang, Y., Zeng, J., Torres, O., Yang, Y., Marshak, A., Reid, J., and Miller, S.: Passive remote sensing of altitude and optical depth of dust plumes using the oxygen A and B bands: First results from EPIC/DSCOVR at Lagrange-1 point, *Geophysical Research Letters*, 44, 7544–7554, <https://doi.org/10.1002/2017GL073939>, 2017.
- Xu, X., Wang, J., Wang, Y., Zeng, J., Torres, O., Reid, J. S., Miller, S. D., Vanderlei Martins, J., and Remer, L. A.: Detecting layer height of smoke aerosols over vegetated land and water surfaces via oxygen absorption bands: Hourly results from EPIC/DSCOVR in deep space, *Atmospheric Measurement Techniques*, 12, 3269–3288, <https://doi.org/10.5194/amt-12-3269-2019>, 2019.
- 860 Yorks, J. E., McGill, M. J., Palm, S. P., Hlavka, D. L., Selmer, P. A., Nowottnick, E. P., Vaughan, M. A., Rodier, S. D., and Hart, W. D.: An overview of the CATS level 1 processing algorithms and data products, *Geophysical Research Letters*, 43, 4632–4639, <https://doi.org/10.1002/2016GL068006>, 2016.
- Yorks, J. E., Wang, J., McGill, M. J., Follette-Cook, M., Nowottnick, E. P., Reid, J. S., Colarco, P. R., Zhang, J., Kalashnikova, O., Yu, H., Marengo, F., Santanello, J. A., Weckwerth, T. M., Li, Z., Campbell, J. R., Yang, P., Diao, M., Noel, V., Meyer, K. G., Carr, J. L., Garay, M., Christian, K., Bennedetti, A., Ring, A. M., Crawford, A., Pavolonis, M. J., Aquila, V., Kim, J., and Kondragunta, S.: A SmallSat Concept
- 865 to Resolve Diurnal and Vertical Variations of Aerosols, Clouds, and Boundary Layer Height, *Bulletin of the American Meteorological Society*, 104, 815–836, <https://doi.org/10.1175/BAMS-D-21-0179.1>, 2023.
- Young, S. A., Vaughan, M. A., Garnier, A., Tackett, J. L., Lambeth, J. D., and Powell, K. A.: Extinction and optical depth retrievals for CALIPSO's Version 4 data release, *Atmospheric Measurement Techniques*, 11, 5701–5727, <https://doi.org/10.5194/amt-11-5701-2018>, 2018.
- 870 Yu, H., Yang, Y., Wang, H., Tan, Q., Chin, M., Levy, R. C., Remer, L. A., Smith, S. J., Yuan, T., and Shi, Y.: Interannual variability and trends of combustion aerosol and dust in major continental outflows revealed by MODIS retrievals and CAM5 simulations during 2003-2017, *Atmospheric Chemistry and Physics*, 20, 139–161, <https://doi.org/10.5194/acp-20-139-2020>, 2020.
- Zhang, H., Kondragunta, S., Laszlo, I., Liu, H., Remer, L. A., Huang, J., Superczynski, S., and Ciren, P.: An enhanced VIIRS aerosol optical thickness (AOT) retrieval algorithm over land using a global surface reflectance ratio database, *Journal of Geophysical Research*, 121,
- 875 717–10, <https://doi.org/10.1002/2016JD024859>, 2016.
- Zhou, Y., Levy, R. C., Remer, L. A., Mattoo, S., and Espinosa, W. R.: Dust Aerosol Retrieval Over the Oceans With the MODIS/VIIRS Dark Target Algorithm: 2. Nonspherical Dust Model, *Earth and Space Science*, 7, <https://doi.org/10.1029/2020EA001222>, 2020a.
- Zhou, Y., Levy, R. C., Remer, L. A., Mattoo, S., Shi, Y., and Wang, C.: Dust Aerosol Retrieval Over the Oceans With the MODIS/VIIRS Dark-Target Algorithm: 1. Dust Detection, *Earth and Space Science*, 7, <https://doi.org/10.1029/2020EA001221>, 2020b.